



Supernova Remnants in M83 as Observed with MUSE

Knox S. Long^{1,2} , William P. Blair³ , P. Frank Winkler⁴ , Lorenza Della Bruna⁵, Angela Adamo⁵ ,
Anna F. McLeod^{6,7} , and Phillippe Amram⁸

¹ Space Telescope Science Institute, 3700 San Martin Drive, Baltimore, MD 21218, USA; long@stsci.edu

² Eureka Scientific, Inc. 2452 Delmer Street, Suite 100, Oakland, CA 94602-3017, USA

³ The William H. Miller III Department of Physics and Astronomy, Johns Hopkins University, 3400 N. Charles Street, Baltimore, MD, 21218, USA; wblair@jhu.edu

⁴ Department of Physics, Middlebury College, Middlebury, VT 05753, USA; winkler@middlebury.edu

⁵ The Oskar Klein Centre, Department of Astronomy, Stockholm University, AlbaNova, SE-10691 Stockholm, Sweden

⁶ Centre for Extragalactic Astronomy, Department of Physics, Durham University, South Road, Durham DH1 3LE, UK

⁷ Institute for Computational Cosmology, Department of Physics, University of Durham, South Road, Durham DH1 3LE, UK

⁸ Aix Marseille Univ, CNRS, CNES, LAM, Laboratoire d'Astrophysique de Marseille, Marseille, France

Received 2021 December 13; revised 2022 February 6; accepted 2022 February 15; published 2022 April 21

Abstract

Here we describe a new study of the supernova remnants (SNRs) and SNR candidates in nearby face-on spiral galaxy M83, based primarily on MUSE integral field spectroscopy. Our revised catalog of SNR candidates in M83 has 366 objects, 81 of which are reported here for the first time. Of these, 229 lie within the MUSE observation region, 160 of which have spectra with [S II]:H α ratios exceeding 0.4, the value generally accepted as confirmation that an emission nebula is shock-heated. Combined with 51 SNR candidates outside the MUSE region with high [S II]:H α ratios, there are 211 spectroscopically confirmed SNRs in M83, the largest number of confirmed SNRs in any external galaxy. MUSE's combination of relatively high spectral resolution and broad wavelength coverage has allowed us to explore two other properties of SNRs that could serve as the basis of future SNR searches. Specifically, most of the objects identified as SNRs on the basis of [S II]:H α ratios exhibit more velocity broadening and lower ratios of [S III]:[S II] emission than H II regions. A search for nebulae with the very broad emission lines expected from young, rapidly expanding remnants revealed none, except for the previously identified B12-174a. The SNRs identified in M83 are, with few exceptions, middle-aged interstellar medium (ISM) dominated ones. Smaller-diameter candidates show a larger range of velocity broadening and a larger range of gas densities than the larger-diameter objects, as expected if the SNRs expanding into denser gas brighten and then fade from view at smaller diameters than those expanding into a more tenuous ISM.

Unified Astronomy Thesaurus concepts: [Supernova remnants \(1667\)](#); [Interstellar medium \(847\)](#)

Supporting material: machine-readable tables

1. Introduction

A large fraction of stars more massive than $8 M_{\odot}$ end their lives as supernovae (SNe) that disrupt all or part of the star, ejecting significant amounts of material at high velocity into the surrounding circumstellar medium (CSM) and interstellar medium (ISM). The interaction of these ejecta in the form of shocks results in emission across a broad range of wavelengths, with the fast primary shock that interacts with the more tenuous medium usually producing X-rays, while secondary shocks driven into the denser phases of the medium emit primarily at ultraviolet, optical, and infrared wavelengths. Most Galactic supernova remnants (SNRs) were initially discovered at radio wavelengths, but most extragalactic SNRs have, for reasons of sensitivity and spatial resolution, been identified using narrow-band (interference-filter) imagery (see, e.g., Long 2017, for a review). More specifically, the vast majority of SNRs in nearby galaxies have been identified as nebulae in which the ratio of [S II] $\lambda\lambda 6716, 6731$:H α emission is greater than 0.4 to separate them from (bright) H II regions, where the ratio is typically 0.1–0.2. The physical basis for this distinction is that there is an extended region behind radiative shocks where S⁺ is the

dominant species of sulfur, while in H II regions, which are photoionized, most sulfur is found in higher ionization states, primarily S⁺⁺.

M83 is a well-studied nearby face-on grand-design spiral galaxy with a starburst nucleus and active star formation along its prominent spiral arms. Because of its proximity (4.61 Mpc; Saha et al. 2006)⁹ and high star formation rate ($3\text{--}4 M_{\odot} \text{ yr}^{-1}$; Boissier et al. 2005), we and our collaborators have conducted a number of searches for SNRs in M83. Beginning with Blair & Long (2004), where 71 SNRs and SNR candidates were identified in M83 using the Dupont telescope at Las Campanas Observatory, members of our team have carried out a series of surveys to compile a more complete and accurate listing of SNRs and SNR candidates in M83, primarily based on optical criteria (Dopita et al. 2010; Blair et al. 2012, 2014). Currently, the most complete published listing was provided by Williams et al. (2019) and includes 278 SNRs and SNR candidates.¹⁰ All of these had appeared in earlier publications.

Many of the SNRs appear to have X-ray counterparts (Long et al. 2014), and a significant number are associated with radio sources (Russell et al. 2020). We have previously confirmed

⁹ We note, in passing, that Della Bruna et al. (2022a, 2022b) have used a somewhat larger distance of 4.9 Mpc due to Jacobs et al. (2009). We have chosen to use 4.61 Mpc to retain consistency with earlier studies on SNRs in M83.

¹⁰ Williams et al. (2019) list a total of 307 objects, but we have removed 29 objects from that list; see below.

103 of the brighter [S II] imaging-selected candidates (out of 118 observed) to have spectroscopic [S II] $\lambda\lambda 6716, 6731$:H α ratios greater than 0.4 using Gemini/GMOS (Winkler et al. 2017). Although the remaining objects observed spectroscopically did not satisfy the standard [S II]:H α criterion, Winkler et al. (2017) suggested that nearly all were still likely SNRs, based on other criteria, such as having coincident X-ray sources and/or significant [O I] emission. From an analysis of the stellar populations in the vicinity of the SNRs (Williams et al. 2019), most are likely the result of core-collapse explosions, as one might expect given the relatively high star formation rate in M83 (Boissier et al. 2005). The vast majority of the SNRs that have been observed spectroscopically appear to be evolved ISM-dominated SNRs, based on characteristics of the emission lines observed. Only two SNRs, one associated with SN 1957D (Long et al. 1989, 2012) and one object, B12-174a, that appears to be the remnant of a missed SN from the last century (Blair et al. 2015), have lines with the (>1000 km s $^{-1}$) velocity widths that are seen in very young Galactic SNRs.

Here we describe an analysis of a new homogeneous set of data on SNRs and SNR candidates in the M83, using the Multi Unit Spectroscopic Explorer (MUSE) on the VLT (Bacon et al. 2010). These observations provide a uniform set of spectro-imaging data covering a significant fraction of the inner bright disk of M83, allowing us to sample all of the SNR candidates in the observed region (both those with and without previous spectra), while also providing more extended spectral coverage than was previously available. Combining the MUSE results with previous data, M83 has the most spectroscopically confirmed SNRs of any galaxy studied to date.

The remainder of this paper is organized as follows: In Section 2, we describe the data used. In Section 3, we compile a new catalog of SNRs and SNR candidates, including a revisit to earlier candidate lists, as well as adding new MUSE and other previously unpublished candidates. In Section 4, we discuss the methodology used to extract the MUSE spectra and compare to previous spectroscopy that overlaps the MUSE mosaic region. In Section 5, we present an overview of the MUSE results, and in Section 6, we discuss the limitations that have developed in applying the primary [S II]:H α ratio criterion for separating SNRs from H II regions. In Section 7, we highlight several individual objects of special interest; in Section 8, we investigate global trends in the MUSE spectra; and in Section 9, we compare the spectra to shock model grids. We summarize our findings in Section 10.

2. Data and Data Reduction

MUSE is an integral field spectrograph mounted on ESO’s VLT in Chile. For the purposes of this paper, we use data obtained from various ESO programs: 096.B-0057(A), 0101.B-0727(A) (PI Adamo), 097.B-0899(B) (PI Ibar), and 097.B-0640(A) (PI Gadotti). These data covered the spectral range 4600–9380 Å with a spectral resolution of about 2.3 Å, which corresponds to a velocity resolution of about 115 km s $^{-1}$ at H α . Individual exposures cover a field of 1’ \times 1’; each spaxel is 0’’2 \times 0’’2 in extent. As described in detail by Della Bruna et al. (2022a), these data have been reprocessed into a single large mosaicked data cube with accurate astrometry and calibration covering the region shown in Figure 1. The median size of point sources in the data cube is 0’’7 (FWHM) at 7000 Å, although there are some slight variations as a function of position and wavelength. To simplify our analysis in the

wavelength range 4600–7760 Å, we have used versions of the data where a stellar continuum has been subtracted using the pPXF fitting code (Cappellari & Emsellem 2004; Cappellari 2017) and the EMILES simple stellar populations (Vazdekis et al. 2016) as described in Della Bruna et al. (2022a). This produced pure emission-line versions of the data cube that made analysis of the nebular emission easier, especially for H β , where the stellar continuum often has fairly obvious stellar absorption features.

M83 has been well observed previously, and these earlier data sets complement the MUSE data in several ways. Magellan imaging (see Figure 1) in excellent (0’’4–0’’5) seeing (Blair et al. 2012) and HST WFC3 multiband imaging (Dopita et al. 2010; Blair et al. 2014) cover the entire area observed with the MUSE mosaic. Soria et al. (2020) describe the detailed HST and multiwavelength characteristics of the complex nuclear region. These higher spatial resolution images can help us understand when the MUSE data may be limited by crowding from nearby sources. Likewise, Gemini GMOS spectroscopy of objects in common with MUSE (Winkler et al. 2017) provides confidence in these new results, which extend to objects much fainter than observed with GMOS.

3. An Updated Catalog of SNRs and SNR Candidates in M83

As we have continued to inspect the HST and Magellan data in the context of other projects, such as our recent radio study of M83 (Russell et al. 2020), we have identified a few additional objects of interest that have not yet appeared in publication. As part of the current project, we also identify a number of new SNR candidates with MUSE (see next subsection). Hence, a goal of this paper is to produce a new baseline catalog of SNRs and SNR candidates for use going forward that includes all of these objects.

In the following subsections, we first discuss the set of new SNR candidates identified uniquely with MUSE from within the MUSE footprint shown in Figure 1. Then, we discuss a few special cases, as well as the previously unpublished candidates, many from the nuclear region that had been set aside in earlier studies. In creating the revised list, we remove from consideration the [O III]-selected list of candidates from Dopita et al. (2010; five objects) or Blair et al. (2012, their Table 3) unless existing data have already confirmed the objects as good SNR candidates; most of the [O III]-selected objects have been shown to be Wolf-Rayet nebulae or other compact H II regions and are no longer considered viable SNR candidates. Some 24 such objects were listed in the Williams et al. (2019) table, as were five historical SNe that do not have known SNR counterparts. These 29 objects have been removed from the new catalog.

3.1. A MUSE Search for Additional Supernova Remnants

As noted earlier, most SNRs in nearby galaxies have been identified using interference-filter imagery. Usually the “H α ” filter passes a significant amount of one or both of the adjacent [N II] $\lambda\lambda 6548, 6583$ lines. Typically, one forms a ratio image by first subtracting a scaled continuum image from the H α and [S II] images and then dividing to create the ratio image that one searches for emission nebulae with higher [S II]:H α ratios than H II regions in the image. Much cleaner ratio images can be created with a high (spectral) resolution integral

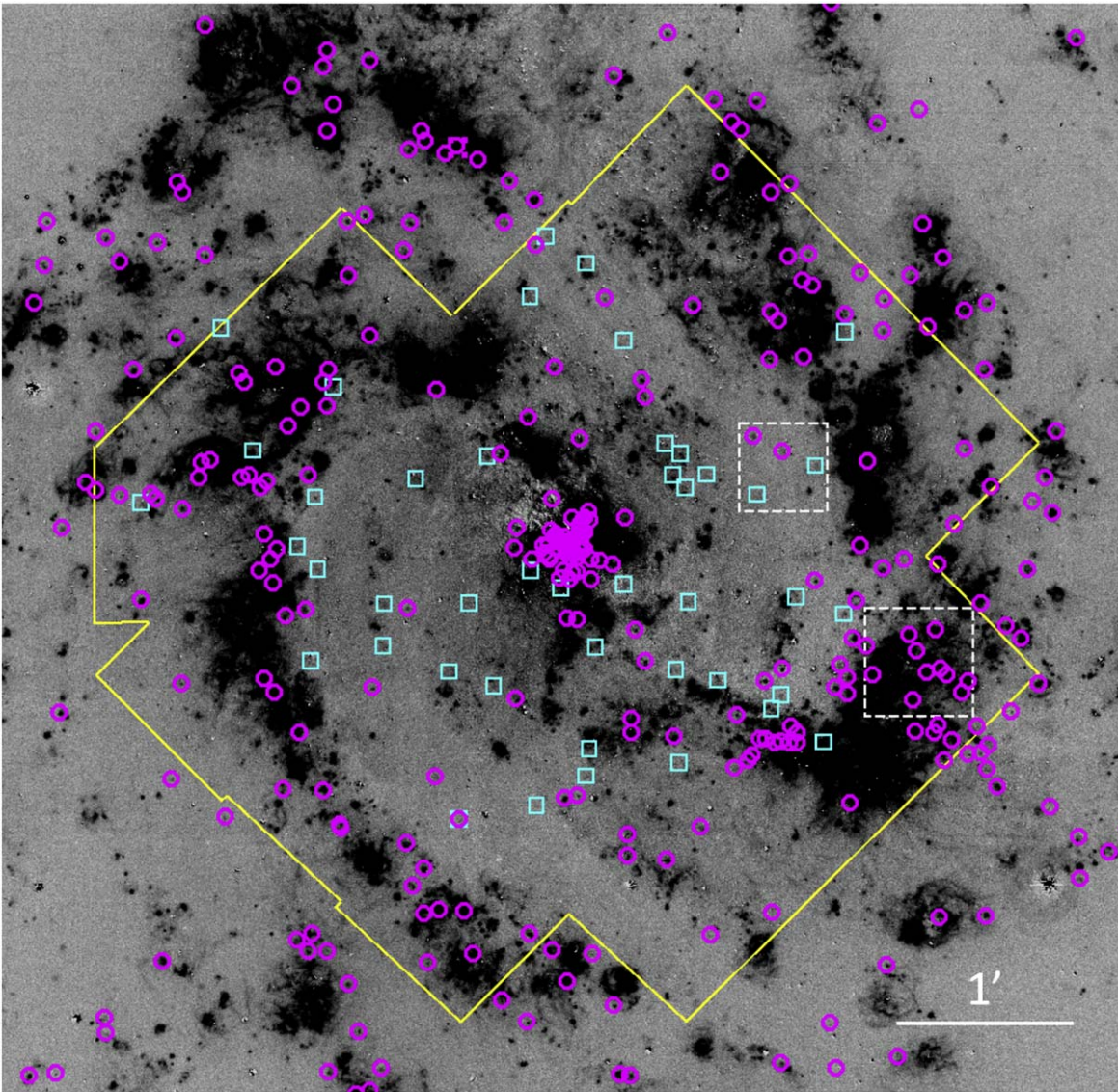


Figure 1. Magellan continuum-subtracted $H\alpha$ image of M83 showing the region covered by the MUSE mosaic in yellow. Magenta circular regions show previous SNR candidates, and cyan square regions show the locations of new SNR candidates identified with MUSE. The MUSE candidates are primarily but not exclusively low surface brightness nebulae discovered in the sampled interarm regions. White dashed boxes show the locations of the regions enlarged in Figure 2 (upper box) and Figure 7 (lower box). A $1'$ scale bar is shown at lower right.

spectrograph like MUSE, since one can exclude the effects of [N II] contamination of $H\alpha$ and one can subtract a continuum on either side of the emission line. In our case, we chose to create the ratio images from using 10 \AA wavelength bands for the two sulfur lines and $H\alpha$, subtracting adjacent continuum bands, and then creating the ratio image. By way of example, a portion of the ratio image is displayed in Figure 2.

Many of the previously known SNRs were of course prominent in this ratio map, as shown by the magenta regions in Figure 2, where the two previously identified objects are detected at significantly higher [S II]: $H\alpha$ ratios than in the Magellan data. However, there were a number of additional locations in the MUSE ratio map that appeared to have elevated ratios; the cyan regions in Figure 2 are two such objects. Indeed, a visual search over the entire MUSE mosaic revealed 44 such objects of interest that passed the following vetting procedure: First, we confirmed that each region showing an elevated ratio had an identifiable $H\alpha$ counterpart by displaying the MUSE $H\alpha$ image alongside the ratio map in

ds9. We then verified that there was, as shown in Figure 2, evidence of the nebulae in our high spatial resolution ($\sim 0''.5$ FWHM) Magellan IMACS emission-line image, but at a level too low to confirm their identity with the previous data. A major reason for this vetting was to avoid the possibility of selecting ill-formed regions of diffuse ionized gas (DIG) to be SNR candidates. These checks combined make us reasonably confident in the selection of these new objects as SNR candidates, i.e., isolated nebulae with higher-than-normal [S II]: $H\alpha$ ratios, and not DIG. They are included in our new catalog. The object B14-48 that Winkler et al. (2017) removed from consideration was already removed from the Williams et al. (2019) list.

In Section 4, we discuss the extraction of MUSE spectra at the positions of the SNRs and SNR candidates in M83, and we confirm that many, but not all, of these new MUSE candidates have [S II]: $H\alpha$ ratios above 0.4, as anticipated from the imaging. On average, objects in this group have derived surface brightnesses toward the lower end of the SNR sample.

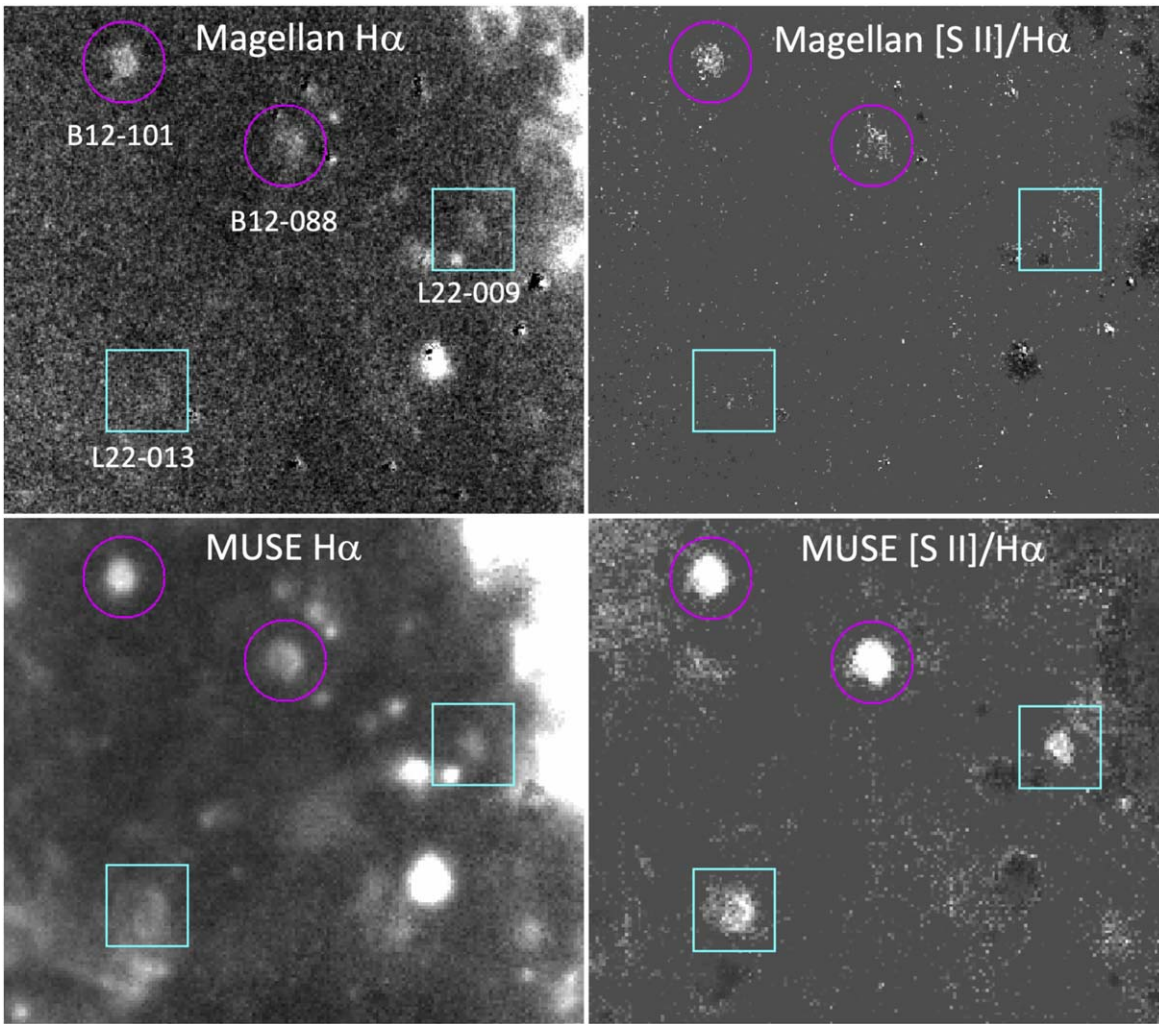


Figure 2. A comparison of $H\alpha$ images and $[S\ II]:H\alpha$ ratio maps for a $30''$ region in M83. The top two panels show previous Magellan IMACS data (Blair et al. 2012), and the bottom two panels show the corresponding data from MUSE. The scaling on the ratio maps is from 0 (black) to 2.0 (white). Thus, lighter values indicate elevated values of the ratio. The magenta circles mark two previously identified SNRs (B12-101 and B12-088), while the cyan squares indicate two additional SNRs identified with MUSE (L22-013 and L22-009). The improved exposure depth and higher S/N in the MUSE data are evident for this relatively sparse interarm field. The previous objects have elevated ratios in the Magellan data but even higher ratios in the MUSE data. The new objects stand out in the MUSE ratio and have identifiable emission counterparts, but they are too marginally detected in the Magellan data to have been identified previously as SNR candidates. For scale, the square regions are $5''$ on a side.

One could imagine pushing observations even lower in surface brightness to possibly find additional SNR candidates, but at some point it becomes impossible to define an actual emission nebula from a slightly brighter patch of DIG in the general ISM. Since the spectral characteristics of the DIG can mimic that of slow shocks, e.g., weak $[O\ III]$ and an enhanced $[S\ II]:H\alpha$ ratio (Galarza et al. 1999; Poetrodjojo et al. 2019; Della Bruna et al. 2022a), it becomes increasingly difficult to distinguish true lower surface brightness SNRs from DIG even with the sensitivity provided with MUSE/VLT. This is discussed further in Section 6.2.

3.2. Other New SNR Candidates and Special Cases

Our ongoing inspection of the Magellan and HST data sets continues to uncover a handful of objects of potential interest that have not been reported previously. Eleven such objects found in the original Magellan imaging data (Blair et al. 2012) are now included in the catalog. Spectroscopy (combined with multiwavelength considerations) occasionally has allowed

some earlier objects to be eliminated from further consideration; Winkler et al. (2017), for example, concluded that the object B14-48 had a low ratio and no other interesting characteristics that pointed to shock heating, so it was dropped.

The largest number of previously unpublished candidates arises from the HST imaging in the nuclear region. Blair et al. (2014) describe the use of the near-IR line of $[Fe\ II]$ $1.644\ \mu m$ as a new shock diagnostic and published a number of M83 SNRs showing this line. However, the situation in the complicated nucleus was set aside and not reported in that analysis. For completeness here, we include 20 new SNR candidates selected using the presence of strong $[Fe\ II]$ emission but little or no optical emission, the vast majority of which are in the nuclear region. Most of these objects are seen in projection against dust lanes and are thought to represent heavily reddened SNRs seen primarily in $[Fe\ II]$.¹¹

¹¹ There are nine other previously published SNRs in the catalog selected on the basis of strong $[Fe\ II]$ emission, so 29 such objects total. A total of 26 of the 29 $[Fe\ II]$ objects are within the MUSE mosaic.

Among the SNR candidates, detailed studies of individual objects have identified a few as microquasars (or candidates) whose spectra also involve shocks. The microquasar MQ1 = D10-N-16 (Soria et al. 2014) is found just NE of the bright nuclear region, and more recently Soria et al. (2020) suggested that two closely spaced SNRs, B12-096 and B12-098, may be two shock-heated lobes of another single microquasar. The latter paper highlighted a handful of other M83 SNR candidates that had peculiar morphology, but none of them panned out as microquasar candidates. We have maintained these three objects in the catalog because they display characteristics of shock heating, but we annotate them for future reference.

3.3. The New Catalog

Our current list of SNRs and SNR candidates in M83 now consists of 366 objects as indicated in Table 1. The catalog includes the 278 nebulae listed by Williams et al. (2019). To this, we have added a total of 87 other nebulae, 81 of which are reported here for the first time: 44 from our search of the MUSE data, and 37 new, previously unpublished candidates from reinspection of the earlier imaging data of the M83 nucleus. Six other objects previously published by Dopita et al. (2010) or Blair et al. (2014) that were considered too marginal to be included in the Williams et al. (2019) list have been reinstated here for completeness. This new catalog composes the largest optical SNR sample available for any single galaxy.

For each object, we list a recommended name; coordinates; an estimated diameter; the distance of the object from the nucleus; the identification of any X-ray sources that are cospatial with the SNR candidate; an indication of whether the object was included in the list of Williams et al. (2019), was seen first in the MUSE data, or has been based on further inspection of the HST or Magellan data; and an indication of whether GMOS or MUSE spectra exist. For some objects, a comment is added. The diameters were measured using the HST images wherever possible; for a relatively small number of low surface brightness, large-diameter objects, the Magellan or MUSE images were used. The galactocentric distances assume an inclination and position angle of 24° and 45°, respectively (Talbot et al. 1979). The X-ray source list utilized is that of Long et al. (2014). Where possible we have used the same names as cited by Williams et al. (2019); completely new objects, L22-001, etc., are in R.A. order (as is the entire table).

4. Extraction of the MUSE Spectra

Of the 366 objects in Table 1, 229 lie within the area outlined by the MUSE mosaic. The primary difference between the sample of objects in and out of the MUSE region is that the MUSE sample contains all of the SNR candidates in the nuclear starburst of the galaxy and all of the objects that were identified on the basis of strong [Fe II] emission. The diameter distribution of the MUSE sample skews somewhat toward smaller-diameter objects; the median (average) diameter of the objects in and out of the MUSE region is 20 (22) pc and 25 (27) pc, respectively, a difference we consider to be inconsequential.

As is apparent from an inspection of Figure 1, many of the SNRs and candidates are located in or near other nebulosity. Consequently, one must allow for the effects of possible contamination when extracting spectra. With such a large number of objects, setting individual regions for background

subtraction is impractical. Hence, we have experimented with a number of more automated approaches for selecting and subtracting background from the spectra. In the analysis that follows, we have used the following procedure. We first extracted the average spectrum from all the spaxels contained within the region centered on the object, with an angular radius of the extraction region given by

$$\theta = \sqrt{\theta_{\text{snr}}^2 + \theta_{\text{psf}}^2}, \quad (1)$$

where θ_{snr} is the angular radius of the SNR measured from high-resolution HST images of the object (see Blair et al. 2014) and θ_{psf} is 0".35.¹² To obtain the local background for subtraction, we first located the spaxel with the lowest H α flux within 5" of the SNR. We then extracted an average background spectrum from the spaxels within 1".5 of that lowest flux spaxel. The net spectrum (with units $\text{ergs cm}^{-2}\text{s}^{-1}\text{\AA}^{-1}\text{ spaxel}^{-1}$) was then obtained by straight subtraction after scaling to the same areal size as the object. As an indication of the resulting data quality, a selection of spectra is shown in Figure 3.

Applying this procedure allowed us to treat the spectral extractions in an automated way, and in general this procedure worked well. (See below for comparison to objects that had prior spectra with Gemini GMOS.) However, we do note that, particularly for faint objects, a different choice of background region would result in different line ratios for individual objects. However, this criticism would apply to almost any choice of background, even one made “by eye.”

With the spectra in hand, we extracted central wavelengths, fluxes, and FWHM for the lines in the various spectra using a custom-built PYTHON script, assuming that the lines had Gaussian shapes. Our purpose-built fitting routine makes use of the CURVE_FIT module of SCIPY.OPTIMIZE, which returns not only the best-fit values but also the covariance matrix. We have used the covariance matrix to establish 1σ error estimates under the assumption that the errors for the various values were uncorrelated. For the doublets, [O III] $\lambda\lambda 4959, 5007$, [O I] $\lambda\lambda 6300, 6364$, and [S II] $\lambda\lambda 6716, 6731$, we fixed the separation of the lines and fit a single FWHM to both lines, which particularly in the case of [O I] and [O III] produced more accurate results for the weaker of the lines in the doublet. H β and [S III] $\lambda 9069$ were treated as singlets.

After some experimentation, we decided to treat the [N II] $\lambda\lambda 6548, 6583$ and H α complex as a single system, fixing the separation between the lines and using a single FWHM. In addition to visually inspecting the results, we carried out a number of checks to validate the fits, including in the cases of typically weaker lines (such as H β , [O III], [O I], and [S III]) that the fitted wavelengths and broadening of the feature were consistent with those of the stronger lines of [N II], H α , and [S II]. To establish upper limits to the flux in cases where the line was not clearly evident, we created versions of the spectra where we artificially added a line of known strength and FWHM at the position of a line. We fit the modified spectrum and used the error in the flux to estimate a 1σ upper limit on a line at the position of the emission lines.

¹² As described by Della Bruna et al. (2022a), there is some variation in the size of the point-spread function over the field. We did not take these changes into account, but we did confirm, by testing different values of the point-spread function, that the exact value of the point-spread function made very little difference in the final results.

Table 1
Supernova Remnants and Candidates in M83

Source name ^a	R.A. (J2000)	Decl. (J2000)	D (pc)	R (kpc)	X-ray ^b	Origin	Spectra	[S II]:H α > 0.4	Comments ^c
B12-001	204.16663	-29.85976	34	6.5	...	W19	GMOS	GMOS	...
B12-002	204.16811	-29.85181	11	6.5	...	W19	none	no	...
B12-003	204.17040	-29.85491	12	6.3	X019	W19	GMOS	GMOS	...
B12-004	204.17292	-29.87107	20	5.9	...	W19	none	no	...
B12-005	204.17325	-29.83230	14	6.8	...	W19	GMOS	GMOS	...
B12-006	204.17638	-29.87149	24	5.7	...	W19	none	no	...
B12-007	204.17801	-29.87637	12	5.5	...	W19	none	no	...
L22-001	204.18136	-29.85193	16	5.5	X029	New	none	no	...
B12-008	204.18208	-29.84608	21	5.6	...	W19	none	no	...
L22-002	204.18240	-29.85858	64	5.3	...	New	none	no	...
B12-009	204.18258	-29.86978	28	5.2	...	W19	none	no	...
B12-010	204.18600	-29.84275	38	5.5	...	W19	GMOS	GMOS	...
B12-011	204.18880	-29.88549	34	4.9	...	W19	none	no	...
B12-012	204.19026	-29.87258	81	4.6	...	W19	GMOS	GMOS	...
B12-013	204.19137	-29.89288	27	4.9	...	W19	none	no	...
B12-014	204.19340	-29.89509	39	4.9	...	W19	GMOS	GMOS	...
B12-015	204.19559	-29.77824	69	8.8	...	W19	none	no	...
B12-016	204.19637	-29.92542	82	6.3	...	W19	none	no	...
B12-017	204.19658	-29.89761	29	4.8	...	W19	none	no	...
B12-018	204.19676	-29.89359	38	4.6	...	W19	none	no	...
B12-019	204.19708	-29.81771	15	6.0	...	W19	none	no	...
B12-020	204.19928	-29.85504	33	4.2	...	W19	GMOS	GMOS	...
B12-021	204.19972	-29.86278	49	4.0	...	W19	GMOS	no	...
B12-022	204.20045	-29.85941	34	4.0	...	W19	GMOS	GMOS	...
B12-023	204.20123	-29.87908	20	3.9	X046	W19	GMOS	GMOS	...
B12-024	204.20188	-29.86172	43	3.9	...	W19	none	no	...
B12-025	204.20245	-29.86814	52	3.8	...	W19	GMOS	GMOS	...
L22-003	204.20312	-29.87479	10	3.7	X048	New	none	no	...
B12-026	204.20414	-29.88169	5	3.8	...	W19	GMOS	GMOS	...
B12-027	204.20469	-29.87358	26	3.6	...	W19	none	no	...
B12-028	204.20569	-29.88887	39	3.9	...	W19	GMOS	no	...
B12-029	204.20641	-29.86030	97	3.5	...	W19	MUSE	no	...
B12-030	204.20669	-29.88491	79	3.7	...	W19	none	no	...
B12-031	204.20676	-29.88713	36	3.8	...	W19	GMOS	GMOS	...
B12-032	204.20680	-29.84290	23	4.1	...	W19	none	no	...
B12-033	204.20700	-29.90115	23	4.4	...	W19	GMOS	GMOS	...
B12-034	204.20716	-29.84921	46	3.8	...	W19	GMOS	GMOS	...
B12-036	204.20754	-29.87138	4	3.4	X053	W19	GMOS	GMOS	...
B12-035	204.20755	-29.88564	31	3.7	...	W19	GMOS	GMOS	...
B14-03	204.20882	-29.87880	14	3.4	...	W19	MUSE	no	[Fe II]

Notes.

^a Source names beginning with B12, B14, and D10 are from Blair et al. (2012, 2014) and Dopita et al. (2010), respectively. Previously unpublished candidates begin with L22.

^b X-ray sources in the Long et al. (2014) list within 1'' of an SNR candidate

^c Objects with the comment [Fe II] were first identified on the basis of detectable [Fe II]1.67 μ m emission.

(This table is available in its entirety in machine-readable form.)

The results are presented in Table 2. As is traditional, we have reported the line strengths relative to a reference H α value, but we provide the H α surface brightness in physical units for scaling purposes. Although we have only presented the FWHM from the H α fits, the FWHMs of all the lines were, within the errors, consistent with one another.

In addition to the spectra of the SNR and SNR candidates, we extracted spectra for 188 other emission nebulae, listed in Table 3, that are more likely to be H II regions. These objects were selected by displaying the MUSE H α image and randomly selecting small isolated patches of H α emission that spanned the surface brightness regime of the SNR candidates in the Williams et al. (2019) list. In choosing the comparison H II regions in this way, we have avoided the bias that might occur

from selecting bright H II regions that are less typical. We also took care to select objects scattered throughout the portion of M83 covered by the MUSE data cube so as not to be biased by local effects. Background subtraction for these objects was performed in a manner similar to that described above for the SNRs. The results of the spectral fits for these H II regions are presented in Table 4.

4.1. Comparison to Previous Spectra

Winkler et al. (2017) used GMOS on Gemini-South to obtain moderate-resolution (3.9 \AA at H α) spectra of 118 of the mostly brighter SNR candidates known previously. Their spectra confirmed that 103 of the objects had [S II]:H α ratios of

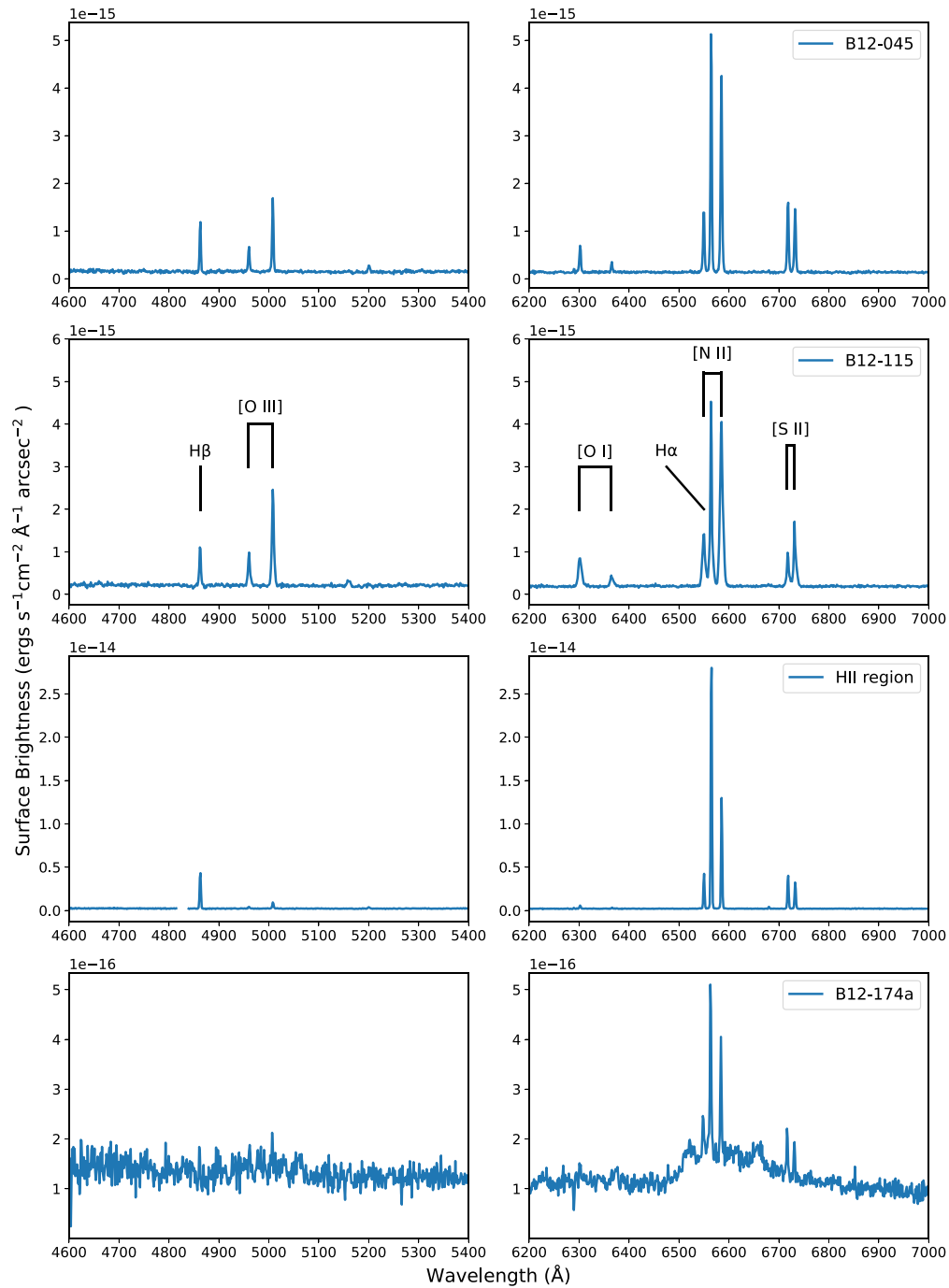


Figure 3. Some example background-subtracted MUSE spectra. The plots have been adjusted to show the lines at rest wavelength. The top two panels show typical SNR spectra, including [O I] $\lambda\lambda 6300, 6364$ in addition to the other red shock indicators (note the high density indicated by the [S II] ratio for B12-115). The third panel shows a typical but comparably faint H II region, for which the forbidden lines are much weaker and [O III] is very weak. Finally, the bottom panel shows the very young SNR B12-174a (Blair et al. 2015), which shows a very broad emission hump in the red. (See text Section 7 for details.) Using MUSE off-band images adjacent to $H\alpha + [N II]$, we were unable to find any other objects with this sort of broad emission profile.

0.4 or larger. Of the objects with lower ratios, most (13) showed evidence of emission from [O I] $\lambda 6300$, nine had [Fe II] $1.644 \mu\text{m}$ emission, and seven were soft X-ray sources. Many of these objects also resided in complex regions of emission, making background subtraction more inaccurate, which could contribute to low observed ratios. In the end, Winkler et al. (2017) argued that all but the aforementioned B14-48 were likely to be SNRs despite their lower observed ratios.

Of the objects with spectra in Winkler et al. (2017), 59 are located within the region studied with MUSE, making a direct

comparison possible. As one might expect, and as shown in Figure 4, there is a fairly good correlation between the [S II]: $H\alpha$ and $H\beta$: $H\alpha$ ratios measured with the two instruments. Not surprisingly, the scatter is much larger for $H\beta$: $H\alpha$ ratios, as $H\beta$ is typically much fainter than the [S II] lines. (Results for [O III] 5007 : $H\beta$ are also similar to those for $H\beta$: $H\alpha$.) Our basic conclusion is that while there are some differences in the individual object line ratios, there is no indication of any systematic issues with the process we have used in extracting and analyzing the spectra.

Table 2
MUSE Spectra of M83 Supernova Remnant Candidates

Source	H α SB ^a	H β ^b	[O III] λ 5007 ^b	[O I] λ 6300 ^b	H α	[N II] λ 6584 ^b	[S II] λ 6716 ^b	[S II] λ 6731 ^b	[S III] λ 9069 ^b	H α FWHM ^c
B12-029	65.5 \pm 0.6	74.6 \pm 2.6	11.6 \pm 5.7	7.5 \pm 3.0	300	101.9 \pm 2.2	51.3 \pm 1.4	33.9 \pm 1.3	3.7 \pm 1.3	2.82 \pm 0.03
B14-03	293.5 \pm 1.2	37.4 \pm 1.1	16.0 \pm 0.7	6.2 \pm 0.7	300	153.9 \pm 1.1	47.5 \pm 0.6	35.8 \pm 0.6	50.7 \pm 0.6	2.58 \pm 0.01
B12-038	28.9 \pm 0.5	61.0 \pm 8.3	0.0 \pm 9.7	26.2 \pm 4.1	300	153.6 \pm 4.6	95.1 \pm 3.9	72.5 \pm 3.7	0.0 \pm 6.0	2.69 \pm 0.05
B12-039	309.2 \pm 1.7	73.5 \pm 1.1	47.2 \pm 0.8	25.0 \pm 0.6	300	224.0 \pm 1.6	120.8 \pm 0.6	90.0 \pm 0.6	9.3 \pm 0.6	3.21 \pm 0.02
B12-040	80.7 \pm 0.5	83.0 \pm 3.6	57.1 \pm 3.2	18.6 \pm 2.1	300	162.3 \pm 1.6	99.3 \pm 1.7	69.4 \pm 1.6	0.0 \pm 1.7	3.19 \pm 0.02
B12-041	85.2 \pm 1.5	55.6 \pm 3.5	76.2 \pm 2.9	27.5 \pm 2.8	300	170.7 \pm 4.8	83.3 \pm 2.3	71.9 \pm 2.2	18.7 \pm 2.5	2.95 \pm 0.05
B12-042	506.2 \pm 3.7	61.0 \pm 0.5	71.6 \pm 0.5	6.0 \pm 0.3	300	142.9 \pm 1.9	63.4 \pm 0.6	48.4 \pm 0.6	16.3 \pm 0.4	2.72 \pm 0.02
B12-043	49.9 \pm 0.6	37.3 \pm 4.8	9.9 \pm 5.2	9.9 \pm 2.9	300	126.5 \pm 3.2	84.7 \pm 2.4	61.8 \pm 2.3	0.0 \pm 4.8	3.22 \pm 0.04
B12-045	176.4 \pm 3.4	59.2 \pm 2.0	123.0 \pm 1.6	44.3 \pm 1.2	300	291.5 \pm 5.7	113.2 \pm 1.5	103.1 \pm 1.5	15.2 \pm 1.4	3.21 \pm 0.05
B12-047	131.3 \pm 2.0	60.8 \pm 2.3	41.6 \pm 2.0	29.3 \pm 1.6	300	197.1 \pm 4.2	105.4 \pm 1.4	79.5 \pm 1.3	7.2 \pm 2.0	3.41 \pm 0.05
B12-048	129.8 \pm 2.5	90.4 \pm 2.3	212.8 \pm 2.9	10.0 \pm 1.6	300	159.2 \pm 5.2	86.2 \pm 2.3	64.4 \pm 2.2	16.6 \pm 2.0	3.61 \pm 0.07
B12-049	166.4 \pm 1.2	72.2 \pm 1.8	54.5 \pm 2.3	11.2 \pm 1.4	300	145.7 \pm 2.0	67.2 \pm 1.3	53.6 \pm 1.2	12.7 \pm 1.1	3.00 \pm 0.02
B12-050	638.5 \pm 3.0	58.5 \pm 0.5	31.4 \pm 0.6	5.7 \pm 0.3	300	143.7 \pm 1.3	50.3 \pm 0.6	37.4 \pm 0.5	16.0 \pm 0.3	2.71 \pm 0.01
B14-08	28.9 \pm 0.6	0.0 \pm 5.4	0.0 \pm 5.1	19.1 \pm 7.6	300	143.2 \pm 5.6	47.5 \pm 3.6	42.4 \pm 3.6	106.5 \pm 5.8	2.35 \pm 0.05
B14-09	1168.5 \pm 2.6	46.8 \pm 0.3	8.1 \pm 0.3	3.7 \pm 0.2	300	126.4 \pm 0.6	40.7 \pm 0.3	32.1 \pm 0.3	25.9 \pm 0.2	2.63 \pm 0.01
B12-053	110.2 \pm 0.9	56.9 \pm 2.2	19.6 \pm 2.6	11.8 \pm 1.3	300	115.7 \pm 2.1	65.9 \pm 1.2	46.0 \pm 1.2	0.0 \pm 1.2	2.77 \pm 0.02
B12-054	182.6 \pm 0.9	70.4 \pm 1.1	19.2 \pm 1.0	10.0 \pm 1.3	300	124.7 \pm 1.2	68.9 \pm 0.6	46.8 \pm 0.6	8.3 \pm 1.0	2.77 \pm 0.01
B14-10	2.8 \pm 0.3	0.0 \pm 45.7	0.0 \pm 42.4	281.8 \pm 88.8	300	115.5 \pm 29.9	95.0 \pm 22.2	51.9 \pm 21.3	0.0 \pm 33.3	2.68 \pm 0.35
B12-056	21.3 \pm 0.6	67.2 \pm 13.5	209.1 \pm 12.6	54.7 \pm 7.1	300	394.0 \pm 8.8	172.7 \pm 6.1	136.9 \pm 5.8	0.0 \pm 5.5	4.11 \pm 0.09
B12-058	36.2 \pm 0.6	59.6 \pm 4.4	77.6 \pm 5.1	42.7 \pm 3.0	300	254.0 \pm 4.4	136.7 \pm 2.6	96.2 \pm 2.4	12.1 \pm 4.5	3.26 \pm 0.05
B12-057	17.8 \pm 0.5	38.1 \pm 8.2	137.6 \pm 11.5	66.6 \pm 8.4	300	364.1 \pm 8.1	185.9 \pm 7.8	122.1 \pm 7.2	0.0 \pm 9.6	4.23 \pm 0.09
B12-060	136.2 \pm 0.7	67.8 \pm 2.7	13.2 \pm 1.8	7.6 \pm 1.3	300	120.2 \pm 1.3	65.9 \pm 1.0	42.4 \pm 1.0	9.0 \pm 1.7	2.93 \pm 0.02
B12-061	109.1 \pm 0.5	77.0 \pm 1.3	15.4 \pm 1.3	10.5 \pm 0.9	300	135.8 \pm 1.2	76.2 \pm 0.7	50.2 \pm 0.7	7.7 \pm 1.2	2.65 \pm 0.01
L22-005	30.7 \pm 0.7	129.4 \pm 12.5	30.6 \pm 10.1	32.5 \pm 13.6	300	68.3 \pm 5.5	27.6 \pm 4.5	69.1 \pm 5.2	22.4 \pm 5.8	2.38 \pm 0.06
B12-062	11.8 \pm 0.5	41.9 \pm 18.4	243.3 \pm 21.7	40.5 \pm 15.7	300	309.3 \pm 12.7	194.7 \pm 13.1	130.7 \pm 12.1	0.0 \pm 10.6	4.47 \pm 0.16
B12-063	8.7 \pm 0.2	79.4 \pm 13.2	215.9 \pm 15.4	39.9 \pm 16.6	300	326.8 \pm 8.2	160.5 \pm 8.1	113.9 \pm 7.5	0.0 \pm 11.6	3.29 \pm 0.08
B12-064	90.8 \pm 0.6	49.3 \pm 3.6	10.5 \pm 2.4	7.8 \pm 2.2	300	164.1 \pm 1.6	72.2 \pm 1.5	53.9 \pm 1.4	17.7 \pm 2.5	2.97 \pm 0.02
B12-065	175.1 \pm 3.8	80.3 \pm 2.9	104.0 \pm 2.6	70.9 \pm 1.8	300	232.0 \pm 6.2	65.1 \pm 1.9	71.3 \pm 1.9	12.8 \pm 1.8	3.82 \pm 0.08
B12-067	119.2 \pm 2.4	61.5 \pm 3.1	150.0 \pm 3.4	43.3 \pm 2.6	300	288.7 \pm 6.0	151.5 \pm 3.2	122.0 \pm 3.0	18.7 \pm 3.2	4.06 \pm 0.07
B12-066	78.8 \pm 1.6	53.3 \pm 5.8	59.5 \pm 5.3	52.6 \pm 4.2	300	356.1 \pm 6.1	107.0 \pm 3.0	116.7 \pm 3.0	20.7 \pm 4.4	4.32 \pm 0.07
L22-006	8.8 \pm 0.4	53.6 \pm 18.3	79.1 \pm 18.6	...	300	247.2 \pm 13.7	170.1 \pm 10.9	127.3 \pm 10.3	0.0 \pm 13.1	2.88 \pm 0.13
B12-069	27.2 \pm 0.6	73.2 \pm 9.6	183.1 \pm 10.6	41.0 \pm 8.3	300	268.9 \pm 6.2	130.6 \pm 5.5	91.5 \pm 5.2	15.0 \pm 6.8	3.18 \pm 0.06
L22-007	24.2 \pm 0.5	51.2 \pm 6.6	93.3 \pm 6.1	34.6 \pm 4.6	300	238.2 \pm 5.8	119.5 \pm 3.3	74.4 \pm 3.0	7.7 \pm 2.9	3.61 \pm 0.07
B12-070	27.1 \pm 0.5	83.6 \pm 16.8	112.1 \pm 11.7	44.8 \pm 8.3	300	260.2 \pm 5.3	142.7 \pm 5.2	107.4 \pm 5.0	15.1 \pm 9.1	3.25 \pm 0.05
B12-071	76.0 \pm 1.1	62.3 \pm 5.6	99.3 \pm 5.6	64.3 \pm 4.5	300	366.6 \pm 4.7	180.4 \pm 3.4	127.8 \pm 3.2	17.1 \pm 4.6	4.92 \pm 0.06
L22-008	196.8 \pm 1.3	60.8 \pm 1.8	7.8 \pm 1.1	12.6 \pm 1.1	300	121.7 \pm 1.8	55.4 \pm 0.9	41.6 \pm 0.9	8.7 \pm 1.1	2.81 \pm 0.02
L22-009	8.2 \pm 0.2	53.4 \pm 15.9	119.1 \pm 14.5	82.9 \pm 11.8	300	338.1 \pm 9.0	160.3 \pm 7.4	115.3 \pm 6.9	0.0 \pm 8.0	4.33 \pm 0.11
B12-074	32.8 \pm 0.5	63.9 \pm 8.0	301.6 \pm 5.0	97.2 \pm 4.3	300	589.5 \pm 5.2	174.7 \pm 3.9	139.1 \pm 3.7	0.0 \pm 2.7	5.01 \pm 0.04
B12-075	250.5 \pm 6.5	61.7 \pm 2.1	87.1 \pm 1.5	66.0 \pm 1.1	300	266.2 \pm 7.6	131.0 \pm 2.1	127.2 \pm 2.1	19.9 \pm 1.2	4.35 \pm 0.10
B12-076	20.8 \pm 0.5	59.6 \pm 13.8	36.8 \pm 8.5	74.6 \pm 7.3	300	251.0 \pm 6.7	133.7 \pm 6.2	119.7 \pm 6.0	10.9 \pm 7.3	3.94 \pm 0.08

Notes.^a Surface brightness in units of 10^{-17} ergs cm⁻² s⁻¹ arcsec⁻².^b Ratio to H α flux where, by convention, H α is normalized to 300.^c In units of Å.

(This table is available in its entirety in machine-readable form.)

Table 3
Comparison H II Regions in M83

Source Name	R.A. (J2000)	Decl. (J2000)	D (pc)	R (kpc)
HII-001	204.20980	-29.85976	30	3.3
HII-002	204.21289	-29.85073	30	3.4
HII-003	204.21551	-29.85977	19	2.9
HII-004	204.21578	-29.85089	26	3.1
HII-005	204.21589	-29.86071	31	2.9
HII-006	204.21708	-29.86958	27	2.7
HII-007	204.21870	-29.87038	23	2.6
HII-008	204.21872	-29.86566	46	2.6
HII-009	204.21901	-29.86967	28	2.5
HII-010	204.22009	-29.87208	36	2.5
HII-011	204.22061	-29.87013	18	2.4
HII-012	204.22193	-29.86755	24	2.3
HII-013	204.22197	-29.87031	40	2.3
HII-014	204.22315	-29.84693	39	2.9
HII-015	204.22358	-29.87392	30	2.3
HII-016	204.22409	-29.86566	27	2.2
HII-017	204.22442	-29.87589	22	2.3
HII-018	204.22455	-29.86160	50	2.2
HII-019	204.22643	-29.86068	37	2.1
HII-020	204.22714	-29.85770	34	2.1
HII-021	204.22726	-29.87350	29	2.0
HII-022	204.22782	-29.89359	37	2.9
HII-023	204.22821	-29.87708	29	2.0
HII-024	204.22863	-29.85969	86	2.0
HII-025	204.22939	-29.85573	33	2.0
HII-026	204.22963	-29.86719	26	1.8
HII-027	204.23233	-29.84877	25	2.2
HII-028	204.23259	-29.83931	23	2.8
HII-029	204.23284	-29.86544	22	1.5
HII-030	204.23351	-29.87683	23	1.7
HII-031	204.23388	-29.86347	26	1.5
HII-032	204.23412	-29.87030	36	1.5
HII-033	204.23531	-29.87662	35	1.6
HII-034	204.23574	-29.84953	28	2.0
HII-035	204.23624	-29.85967	33	1.4
HII-036	204.23625	-29.87032	36	1.3
HII-037	204.23697	-29.88843	32	2.2
HII-038	204.23699	-29.88010	67	1.7
HII-039	204.23702	-29.86251	26	1.3
HII-040	204.23703	-29.85281	27	1.7

Note. This table (with 188 rows) is available in its entirety in machine-readable form.

(This table is available in its entirety in machine-readable form.)

Having said this, we note that there does appear to be a tendency for objects that exceed an [S II]:H α ratio of 0.4 in the MUSE spectra to have even higher values of the ratio in the GMOS spectra. This would be the sense if the GMOS slit observations were more effectively allowing local contamination to be subtracted. However, the differences could also be due to the fact that in the case of the MUSE spectra the spaxels used in creating the source and background spectra were created by a mechanical process based on the size of the source and the point-spread function, whereas the Winkler et al. (2017) GMOS extractions were carried out using source and background regions that were selected individually for each object.

5. Results

Applying the traditional [S II]:H α criterion to the objects within the MUSE footprint, we find the following: Of the 229

objects within the MUSE field that have previously been classified as SNRs on the basis of narrowband imagery, 160 have MUSE-determined [S II]:H α ratios of 0.4 or greater, and 187 have ratios greater than 0.3. By contrast, for the random sample of 188 H II regions, only seven have a ratio of 0.4 or more, and 26 have a ratio greater than 0.3. The median value of the ratio is 0.62 for the SNR sample and 0.20 for the H II region sample. The latter value is higher than the value of 0.1 that is typically quoted for H II regions, but that value is more applicable to high surface brightness H II regions.

Figure 5 shows the derived [S II]:H α ratios as a function of H α surface brightness and as a function of deprojected galactocentric distance for both the SNRs and H II region samples. There is an obvious trend for the SNRs to have higher ratios at lower surface brightnesses, although there is a large dispersion. This is, for the most part, a selection effect that results from how the sample was constructed; it is easier to identify bright objects with elevated ratios than faint ones, so in the case of the faint objects one actually “needs” a higher ratio to pick out the object. At the high surface brightness end of the distribution, a number of the SNR candidates have MUSE-derived ratios below 0.4; most of these objects still seem to be elevated relative to H II regions of comparable surface brightness, but the distinction is less clear. Most of these objects have soft X-ray counterparts or other indicators that help to solidify the SNR identifications. Still, this points to a limitation in blindly applying the [S II]:H $\alpha \geq 0.4$ criterion across the board, a topic that is discussed more thoroughly in Section 6 below.

Observationally, it is clear that the nebulae selected to be H II regions generally have [S II]:H α ratios that are near [S II]:H $\alpha = 0.2$, although there is a trend for lower surface brightness H II regions to have more elevated ratios, even approaching or exceeding the nominal 0.4 ratio discriminant for shock heating. However, the low surface brightness SNR sample trends toward even higher values of the ratio as well, thus largely maintaining a separation from the H II regions of similar surface brightness. We thus maintain confidence that most of these faint SNR candidates are viable.

As shown in the right panel of Figure 5, there are no obvious trends in the [S II]:H α ratio as a function of galactocentric distance in either the SNR or H II region samples. There is a tendency for the SNRs in the nuclear region to have systematically lower ratios. There are 48 candidates with galactocentric distances less than 0.5 kpc; of these, only 20 (or 42%) have [S II]:H α ratios greater than 0.4. There are 181 candidates farther from the nucleus; 140 (or 77%) satisfy the [S II]:H α criterion. This is not unexpected; a number of the SNR candidates in the nuclear region were selected primarily on the basis of the [Fe II] emission and were quite faint in H α . Additionally, background subtraction is more difficult in the very complex nuclear region.¹³

The extended red spectral coverage of the MUSE spectra and the ~ 100 km s $^{-1}$ spectral resolution allow us to look at these samples in additional ways. The left panel of Figure 6 uses the [S III] $\lambda 9069$ line in ratio with [S II] and compares this against the [S II]:H α ratio to show something quite interesting. As

¹³ As noted earlier, Winkler et al. (2017) obtained GMOS spectra showing that 103 of 118 SNR candidates have [S II]:H α ratios greater than 0.4, a success rate of 87%. The lower success rate obtained with MUSE is due primarily to the fact that the MUSE sample includes the SNRs in the nuclear region, and secondarily to the fact that the MUSE spectra include both bright and faint SNRs in the field of view, whereas objects in the GMOS study were selected at some level to be bright.

Table 4
MUSE Spectra of M83 H II Regions

Source	H α SB ^a	H β ^b	[O III] λ 5007 ^b	[O I] λ 6300 ^b	H α	[N II] λ 6584 ^b	[S II] λ 6716 ^b	[S II] λ 6731 ^b	[S III] λ 9069 ^b	H α FWHM ^c
HII-001	54.4 ± 0.4	59.2 ± 5.5	0.0 ± 3.2	4.9 ± 14.6	300	66.5 ± 1.6	27.3 ± 1.8	21.7 ± 1.7	7.2 ± 3.2	2.40 ± 0.02
HII-002	40.3 ± 0.4	64.8 ± 4.0	0.0 ± 3.9	23.8 ± 3.1	300	90.9 ± 2.6	33.8 ± 2.5	22.1 ± 2.3	14.8 ± 3.4	2.53 ± 0.03
HII-003	47.0 ± 0.4	66.8 ± 4.8	5.7 ± 3.1	0.0 ± 4.7	300	103.0 ± 2.2	52.6 ± 1.9	40.0 ± 1.8	7.6 ± 2.9	2.65 ± 0.02
HII-004	38.7 ± 0.4	32.3 ± 4.2	33.1 ± 8.6	0.0 ± 5.7	300	138.1 ± 3.0	46.0 ± 2.3	38.5 ± 2.2	28.7 ± 3.2	2.79 ± 0.03
HII-005	55.0 ± 0.3	58.1 ± 3.4	15.3 ± 3.6	8.8 ± 1.7	300	131.7 ± 1.6	39.1 ± 1.6	29.1 ± 1.5	17.7 ± 2.0	2.58 ± 0.02
HII-006	23.4 ± 0.2	65.6 ± 5.7	11.0 ± 5.4	0.0 ± 8.3	300	135.4 ± 2.7	35.8 ± 2.4	25.0 ± 2.2	0.0 ± 4.0	2.74 ± 0.03
HII-007	92.0 ± 0.4	67.2 ± 1.7	4.5 ± 1.1	3.2 ± 1.3	300	109.3 ± 1.0	23.4 ± 0.8	17.3 ± 0.7	8.6 ± 1.2	2.63 ± 0.01
HII-008	94.8 ± 0.3	45.1 ± 1.3	4.8 ± 1.2	1.2 ± 0.9	300	100.3 ± 0.9	32.1 ± 0.7	23.5 ± 0.6	11.8 ± 0.8	2.62 ± 0.01
HII-009	31.3 ± 0.2	78.8 ± 5.4	14.7 ± 4.8	11.1 ± 2.6	300	178.7 ± 2.1	49.3 ± 2.1	34.0 ± 2.0	0.0 ± 3.0	2.61 ± 0.02
HII-010	251.5 ± 0.9	50.0 ± 0.4	8.0 ± 0.4	1.5 ± 0.3	300	149.2 ± 1.0	30.8 ± 0.3	22.2 ± 0.3	20.8 ± 0.4	2.56 ± 0.01
HII-011	9.4 ± 0.3	0.0 ± 14.5	0.0 ± 12.4	43.6 ± 11.0	300	207.6 ± 9.3	95.3 ± 7.3	56.6 ± 6.6	0.0 ± 11.4	2.95 ± 0.10
HII-012	23.9 ± 0.2	63.7 ± 6.5	0.0 ± 4.0	9.1 ± 8.5	300	122.0 ± 2.5	40.3 ± 3.0	25.0 ± 2.8	0.0 ± 4.8	2.60 ± 0.03
HII-013	363.5 ± 1.1	71.0 ± 0.5	8.6 ± 0.3	1.2 ± 0.2	300	122.1 ± 0.8	22.6 ± 0.3	16.2 ± 0.3	15.6 ± 0.3	2.51 ± 0.01
HII-014	46.1 ± 0.4	59.5 ± 5.3	67.4 ± 4.3	18.2 ± 2.6	300	115.5 ± 2.4	45.9 ± 2.3	26.0 ± 2.0	27.7 ± 2.3	2.53 ± 0.03
HII-015	22.7 ± 0.4	63.4 ± 8.9	10.2 ± 5.7	57.1 ± 6.1	300	79.5 ± 4.0	37.0 ± 3.7	25.1 ± 3.4	0.0 ± 5.3	2.75 ± 0.05
HII-016	65.0 ± 0.4	54.1 ± 2.4	6.7 ± 2.0	0.0 ± 3.0	300	89.3 ± 1.5	28.7 ± 1.2	20.7 ± 1.1	11.4 ± 1.5	2.51 ± 0.02
HII-017	33.3 ± 0.5	37.3 ± 6.8	0.0 ± 5.3	17.0 ± 7.0	300	98.8 ± 3.6	33.9 ± 3.2	25.0 ± 3.1	0.0 ± 5.7	2.56 ± 0.04
HII-018	7.6 ± 0.2	0.0 ± 11.8	190.1 ± 16.1	12.1 ± 14.2	300	212.2 ± 7.6	82.9 ± 7.6	52.3 ± 6.9	70.7 ± 14.2	2.47 ± 0.06
HII-019	59.6 ± 0.3	68.2 ± 2.8	8.0 ± 1.8	4.7 ± 1.3	300	159.3 ± 1.3	40.3 ± 0.9	25.1 ± 0.8	18.7 ± 1.7	2.66 ± 0.01
HII-020	8.7 ± 0.2	75.1 ± 11.6	0.0 ± 9.4	22.4 ± 4.8	300	103.0 ± 5.6	27.1 ± 5.8	17.6 ± 5.3	0.0 ± 7.7	2.58 ± 0.06
HII-021	55.0 ± 0.4	57.8 ± 2.3	7.0 ± 2.4	4.5 ± 1.5	300	137.9 ± 1.7	35.8 ± 1.4	25.1 ± 1.3	8.8 ± 2.0	2.62 ± 0.02
HII-022	200.9 ± 0.9	73.8 ± 1.4	4.3 ± 1.0	1.6 ± 0.7	300	76.9 ± 1.1	28.7 ± 0.6	19.2 ± 0.5	7.5 ± 0.9	2.55 ± 0.01
HII-023	12.4 ± 0.3	49.0 ± 13.4	38.7 ± 19.4	0.0 ± 17.4	300	129.4 ± 6.7	62.2 ± 7.2	45.1 ± 6.8	0.0 ± 8.6	2.74 ± 0.08
HII-024	4.7 ± 0.2	0.0 ± 15.4	0.0 ± 14.0	0.0 ± 40.3	300	83.5 ± 9.7	62.4 ± 8.7	37.1 ± 7.9	0.0 ± 13.2	2.61 ± 0.12
HII-025	5.8 ± 0.2	30.7 ± 13.2	0.0 ± 12.9	29.6 ± 13.4	300	82.0 ± 8.1	62.0 ± 8.5	46.1 ± 8.0	0.0 ± 11.3	2.49 ± 0.09
HII-026	10.4 ± 0.3	142.8 ± 25.2	45.9 ± 12.5	30.7 ± 14.6	300	175.1 ± 6.9	64.2 ± 7.5	53.0 ± 7.2	0.0 ± 10.1	2.60 ± 0.07
HII-027	79.3 ± 0.5	54.8 ± 2.5	70.7 ± 1.9	17.2 ± 1.5	300	106.6 ± 1.5	28.1 ± 1.3	22.6 ± 1.2	28.6 ± 1.8	2.61 ± 0.02
HII-028	48.4 ± 0.4	65.4 ± 4.7	15.0 ± 4.9	0.0 ± 6.6	300	137.2 ± 2.4	43.4 ± 2.0	34.6 ± 1.9	22.9 ± 2.5	2.68 ± 0.03
HII-029	13.1 ± 0.3	84.0 ± 11.3	16.2 ± 7.7	21.0 ± 8.1	300	107.2 ± 5.1	43.0 ± 5.3	38.3 ± 5.2	0.0 ± 7.6	2.49 ± 0.06
HII-030	53.5 ± 0.6	92.6 ± 6.4	90.7 ± 4.4	12.0 ± 4.3	300	210.1 ± 3.0	37.5 ± 2.8	31.9 ± 2.7	30.6 ± 3.9	2.65 ± 0.03
HII-031	7.5 ± 0.2	92.7 ± 13.5	628.3 ± 14.0	36.0 ± 14.0	300	107.4 ± 8.0	31.3 ± 6.6	50.1 ± 7.2	0.0 ± 10.1	3.13 ± 0.11
HII-032	66.1 ± 0.3	68.5 ± 2.5	3.1 ± 2.0	5.0 ± 1.5	300	99.9 ± 1.3	29.1 ± 1.0	19.6 ± 1.0	7.0 ± 1.4	2.61 ± 0.01
HII-033	5.7 ± 0.6	450.3 ± 133.5	0.0 ± 33.1	0.0 ± 40.0	300	310.4 ± 31.8	97.9 ± 29.7	37.0 ± 25.6	0.0 ± 34.4	3.30 ± 0.30
HII-034	24.6 ± 0.2	73.4 ± 5.4	0.0 ± 3.8	0.0 ± 8.3	300	103.7 ± 2.4	49.8 ± 2.0	29.4 ± 1.8	9.7 ± 3.7	2.70 ± 0.03
HII-035	28.7 ± 0.2	69.5 ± 3.2	0.0 ± 2.1	0.0 ± 6.3	300	62.5 ± 1.8	19.8 ± 1.5	10.3 ± 1.4	8.6 ± 1.6	2.49 ± 0.02
HII-036	35.6 ± 1.3	80.4 ± 4.3	30.6 ± 6.9	9.4 ± 4.0	300	324.4 ± 11.3	28.6 ± 1.9	21.3 ± 1.8	0.0 ± 2.5	5.40 ± 0.17
HII-037	70.1 ± 0.5	80.8 ± 3.4	0.0 ± 2.4	0.0 ± 3.1	300	65.1 ± 1.8	22.5 ± 1.5	15.1 ± 1.3	0.0 ± 2.2	2.62 ± 0.02
HII-038	1571.5 ± 4.5	37.8 ± 0.2	4.6 ± 0.2	0.7 ± 0.1	300	124.1 ± 0.7	22.7 ± 0.3	17.5 ± 0.3	40.5 ± 0.1	2.52 ± 0.01
HII-039	132.7 ± 0.3	66.3 ± 0.8	3.2 ± 0.5	2.3 ± 0.5	300	116.8 ± 0.6	23.7 ± 0.3	16.3 ± 0.3	14.7 ± 0.4	2.49 ± 0.01
HII-040	7.5 ± 0.2	65.2 ± 13.0	0.0 ± 9.3	0.0 ± 25.4	300	144.1 ± 7.3	51.0 ± 6.2	31.4 ± 5.9	0.0 ± 9.5	2.53 ± 0.08

Notes.

^a Surface brightness in units of 10^{-17} ergs cm⁻² s⁻¹ arcsec⁻².

^b Ratio to H α flux where, by convention, H α is normalized to 300.

^c In units of Å.

(This table is available in its entirety in machine-readable form.)

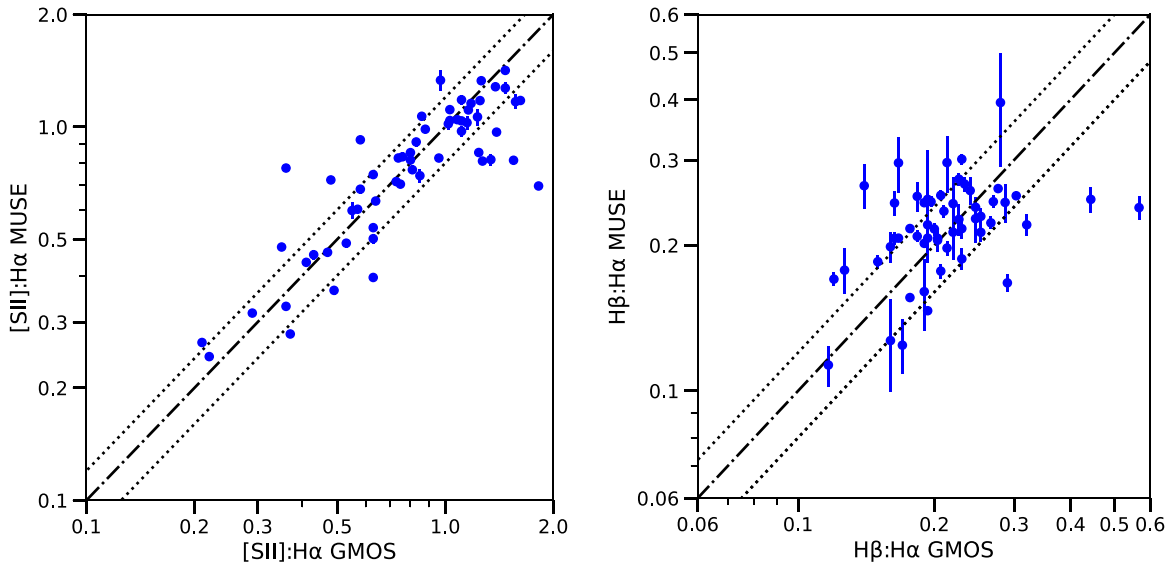


Figure 4. Left: a comparison of [S II]:H α ratios of SNRs observed with GMOS and MUSE. Right: a comparison of H β :H α ratios of the SNRs. Ideally all of the values would lie along the “dotted–dashed” curves, but modest scatter is present. The “dotted” lines show the locus for a 20% difference between the measurements with GMOS and MUSE, and most of the points are encompassed. The main outliers in the left panel show higher ratios in the GMOS data, consistent with better isolation and less contamination in these slitted observations. The weakness of H β (and hence larger uncertainties) accounts for the scatter seen in the right panel.

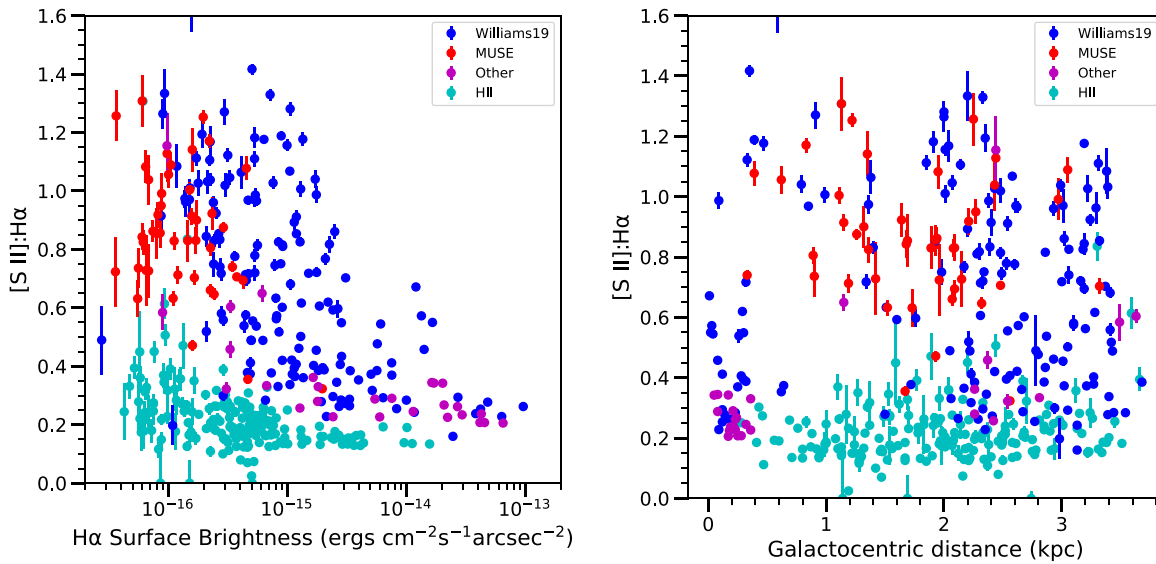


Figure 5. Left: the MUSE-derived [S II]:H α ratio as a function of H α surface brightness for objects in our catalogs. Objects shown in blue were in the Williams et al. (2019) list of SNRs and SNR candidates, while purple shows results for some of the additional candidates described in Section 3. Also shown in red are the newly identified MUSE SNR candidates, which, as expected, trend toward the lower surface brightnesses. Results from the H II region sample are shown in turquoise. Right: [S II]:H α ratio as a function of galactocentric distance. The 1σ errors in the [S II]:H α ratios are shown. No particular trends are seen, nor were they expected, in this plot. Note that the newly identified MUSE SNRs look entirely consistent with the earlier sample.

noted earlier, S⁺⁺ is the dominant species of sulfur in H II regions, whereas S⁺ is prominent in the recombination and cooling zones of shocks. As expected, those objects selected as H II regions trend toward significantly higher [S III]:[S II] ratios. In fact, 58% of the H II region sample has a [S III]:[S II] ratio greater than 0.1, whereas only 10% of the SNR sample does. While [S III] can be seen in SNR spectra (just like [O III], depending on shock velocity), the much stronger [S II] emission from the recombination zone of the shocks forces the SNR [S III]:[S II] ratios to be systematically lower. The separation is not clean, however, and a number of objects are in an overlapping region in the lower left corner of the plot. We note that no correction for differential extinction has been made

here; a correction would only increase the relative strength of [S II] and drive sources toward lower [S III]:[S II] ratios. While the near-IR region containing the [S III] line is not often observed for SNRs, it appears that the [S III]:[S II] ratio offers a secondary diagnostic that can help determine the ionization character of uncertain objects. A possible advantage of the [S III]:[S II] ratio as a shock discriminator is that it involves only a single element and therefore is not sensitive to questions of relative abundance.

As recently emphasized by Points et al. (2019), with sufficiently high spectral resolution, SNRs (at least ones with significant shock velocities) can be separated from H II regions kinematically on the basis of their line widths. Indeed,

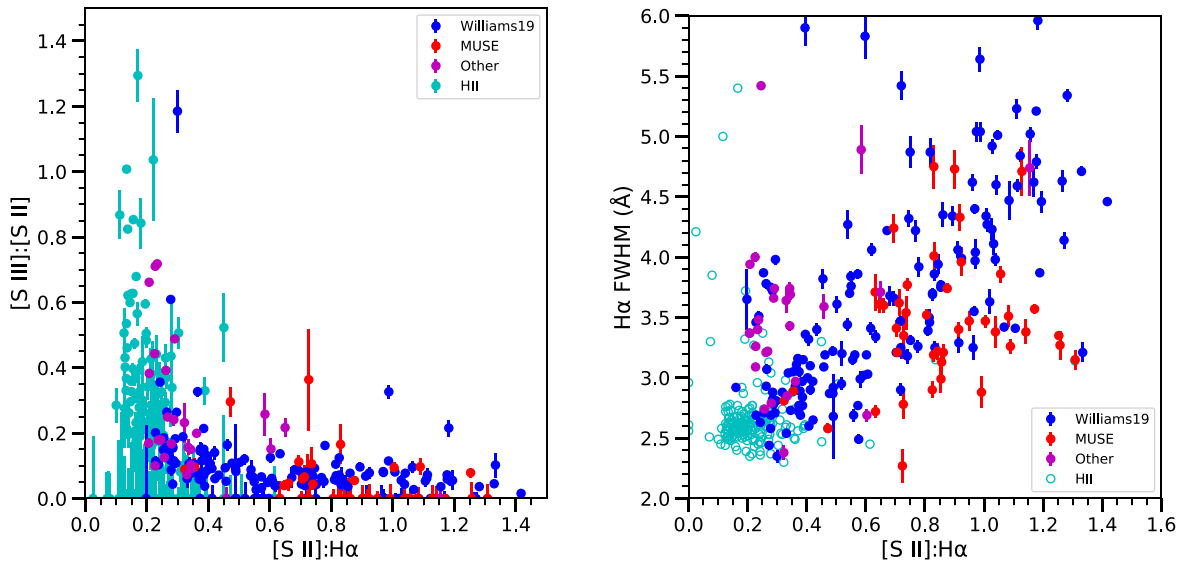


Figure 6. Left: $[S\ III]:[S\ II]$ as a function of the $[S\ II]:H\alpha$ ratio. SNRs trend toward low values of this ratio. Objects where no $[S\ III]$ was detected lie along the x-axis with 1σ upper limits on the ratio. Right: the FWHM of $H\alpha$ as a function of the $[S\ II]:H\alpha$ ratio. SNRs tend to have broadened line profiles owing to bulk motions of the shocked gas. For the SNRs, 1σ errors on the fitted FWHM are shown. Colors are the same as in Figure 5.

McLeod et al. (2021) have used MUSE spectra to confirm a number of SNRs in NGC 300. The utility of measuring line widths is also evident in the MUSE spectra of M83 SNRs and candidates. In the right panel of Figure 6, we show the derived FWHM values for the $H\alpha$ line from our simple Gaussian fits. Here, with the exception of a handful of objects, there is good separation between the SNRs, which show signs of broadening, and H II regions, which effectively scatter around the instrumental resolution of $\sim 2.3\text{ \AA}$. For the SNR sample, 68% of the SNR candidates have $H\alpha$ line widths that exceed 3 \AA , whereas only 5% of the objects in the H II region sample do. The H II region outliers can be attributed to very low surface brightness objects with poorly determined line widths. The SNRs at the lowest FWHM values have slow shocks, or their spectra are contaminated by H II emission such that the higher-velocity emission is masked. This discriminant works well despite the fact that significant dispersion is present within the SNR sample itself. We also note that the newly determined MUSE SNR sample (red points) looks similar to the earlier objects from the Williams et al. (2019) catalog in both of the $[S\ III]:[S\ II]$ and kinematic diagnostics.

Another well-known shock indicator is the $[O\ I]:H\alpha$ ratio, which, as recently emphasized by Kopsacheili et al. (2020), should be near zero in photoionized gas but with apparent $[O\ I]$ emission in shocked gas. In M83, as a result of its recession velocity, the $[O\ I]$ doublet in M83 is fairly well separated from $[O\ I]$ in the airglow. Two-thirds of the SNR candidates have $[O\ I]:H\alpha \geq 0.1$. Interestingly, there are no SNR candidates with $[S\ II]:H\alpha < 0.4$ that have $[O\ I]:H\alpha \geq 0.1$, indicating that these low-ionization lines tend to track one another.

We can summarize these results as follows: If an SNR candidate has $[S\ II]:H\alpha \geq 0.4$, there are usually other indicators of shock heating that support its identification as an SNR. Of the 160 SNRs satisfying the $[S\ II]:H\alpha \geq 0.4$ criterion, 154 have $[S\ III]:[S\ II] < 0.2$, 113 have $[O\ I]:H\alpha \geq 0.1$, and 137 have $H\alpha$ FWHM $\geq 3\text{ \AA}$. However, we also note that many of the SNR candidates that fail the $[S\ II]:H\alpha$ criterion would pass as SNRs based on relatively weak $[S\ III]$ emission and/or evidence of velocity-broadened lines. Of the 69 SNR candidates that fail

the $[S\ II]:H\alpha$ criterion, 48 have $[S\ III]:[S\ II] < 0.2$, and 34 have $H\alpha$ FWHM $\geq 3\text{ \AA}$. One way to interpret this would be to argue that a number of the objects observed to be below the $[S\ II]:H\alpha$ threshold are indeed likely to be SNRs.

By comparison, in the 188-object H II region sample, 181 have $[S\ II]:H\alpha < 0.4$, so one would expect little contamination with the SNR sample. However, 97 of these objects have $[S\ III]:[S\ II] < 0.2$, 11 have $[O\ I]:H\alpha \geq 0.1$, and 11 have $H\alpha$ FWHM $\geq 3\text{ \AA}$, all more similar to the SNR sample. Of the seven H II objects that have $[S\ II]:H\alpha \geq 0.4$, six have $[S\ III]:[S\ II] < 0.2$, three have $[O\ I]:H\alpha \geq 0.1$, and three have $H\alpha$ FWHM $\geq 3\text{ \AA}$ and thus have SNR-like characteristics. Since these faint H II regions were selected “by eye” looking only at the MUSE $H\alpha$ data, indications are that a small amount of confusion in the sample is likely at the lowest surface brightnesses sampled.

Another largely independent indicator that an emission nebula is an SNR is evidence of X-ray emission, since H II regions (though not necessarily the X-ray binaries that can be found in them) are relatively faint in X-rays. A total of 108 of the SNR candidates in our SNR catalog lie within $1''$ of an X-ray source identified by Long et al. (2014) in M83. Shifting the positions of the sources in random directions and recalculating the number of spatial coincidences suggests that no more than 10 of these coincidences are expected by chance. Of these, 74 were in the regions observed with MUSE, and 54 of those have $[S\ II]:H\alpha \geq 0.4$.

One way to identify SNRs is through the hardness of the X-ray spectra. As discussed by Long et al. (2014), SNRs are soft X-ray sources compared to the other types of sources, such as X-ray binaries and background active galactic nuclei, that are typically seen in X-ray surveys of nearby galaxies, including M83. Long et al. (2014) characterized the X-ray spectra of M83 sources in terms of a hardness ratio of the form $(M - S)/T$, where S is the counts observed between 0.35 and 1.1 keV, M between 1.1 and 2.6 keV, and T between 0.35 and 8 keV. This ratio is expected to vary roughly from -1 for a source with counts only in the S band to $+1$ for sources with counts only in the M band.

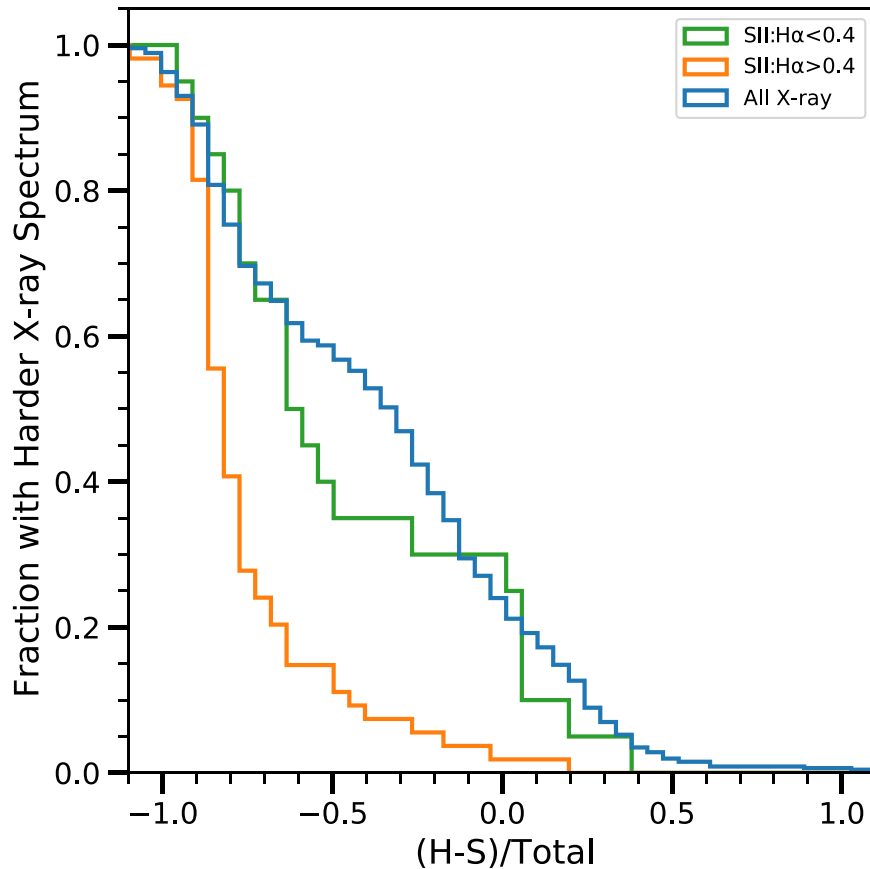


Figure 7. The fraction of X-ray sources with hardness ratios $(M - S)/T$ greater than a given value for all the sources in the X-ray sample, for sources spatially coincident with SNR candidates with $[S II]:H\alpha \geq 0.4$ and for those with ratios less than 0.4.

As shown in Figure 7, the 54 objects with coincident X-ray sources and $[S II]:H\alpha \geq 0.4$ are systematically softer in X-rays than the general X-ray source population in M83, which strengthens the case that these sources are actually SNRs. On the other hand, the distribution of hardness ratios of the SNR candidates with $[S II]:H\alpha < 0.4$ is very different, which suggests, but does not prove (given that the sample contains only 20 objects), that most of these objects are not SNRs. To make this somewhat more quantitative, a Kolmogorov–Smirnov test of the hypothesis that the hardness ratios of SNRs with $[S II]:H\alpha \geq 0.4$ are drawn from the same population as the entire X-ray sample is disproven with a probability of 1.3×10^{-10} , but the same test results in a value of 0.28 for the objects with $[S II]:H\alpha < 0.4$.

In principle, radio emission also provides a straightforward way to distinguish H II regions and SNRs. Indeed, most Galactic SNRs were first identified as extended, nonthermal X-ray sources. In the case of M83, Russell et al. (2020) identified 270 individual radio sources in M83 (outside of the complex nuclear region) using ATCA. Of these, 62 lie within $1''$ of the current sample of SNR candidates in M83, whereas seven would have been expected by chance. There are 38 of these objects with MUSE spectra, and 26 (or 68%) have $[S II]:H\alpha \geq 0.4$, which is fairly similar to the fraction that have high $[S II]:H\alpha$ ratios in the entire MUSE sample. Russell et al. (2020) hoped to use their radio data to identify SNRs in M83, but, unfortunately, they found that the radio spectral indices derived from their data were not accurate enough to separate thermal and nonthermal radio sources. Hence, the existing catalog is of limited utility in determining whether any

particular SNR candidate is actually an SNR. Hopefully a radio survey that delivers reliable spectral indices will be conducted in the not-too-distant future.¹⁴

6. Limitations of the $[S II]:H\alpha$ Ratio Criterion

It is worth revisiting the history of using the $[S II]:H\alpha$ ratio as a primary shock diagnostic. Although Mathewson & Clarke (1973) and other early researchers proposed the strengths of $[S II]$ lines relative to $H\alpha$ as an optical criterion for distinguishing SNRs from H II regions, D’Odorico (1978) appears to have been the first to propose using the specific ratio of $[S II]:H\alpha = 0.4$ as the observational dividing line between shock-heated and photoionized gas. This criterion was then adopted by Blair et al. (1981) in their early study of SNRs in M31, and in many other studies going forward. The expectation of enhanced $[S II]:H\alpha$ ratios was also vetted by many early shock model calculation grids, such as those of Raymond (1979) and Shull & McKee (1979), although a specific dividing line of 0.4 was not called out. Indeed, close inspection of these models, or more recent grids of shock models that cover a broad parameter space such as those of Allen et al. (2008), shows that there are indeed shock conditions for which $[S II]:H\alpha$ ratios below 0.4 can result. The application of this criterion

¹⁴ Russell et al. (2020) carried out a more sophisticated analysis of spatial coincidences than we have done here that accounted for the apparent sizes of the radio sources. They identified 64 in unconfused regions based on the Williams et al. (2019) list of SNR candidates. To avoid future confusion and because of the limited utility of the present radio spectral data, we have chosen not to include radio coincidences in Table 1.

has been widely successful not so much because of the specific value of 0.4 but because observationally there has been a large gap between the typical low $[\text{S II}]:\text{H}\alpha$ ratios seen in photoionized gas and the enhanced ratios well in excess of 0.4 observed in many SNRs. In recent studies over the past decade, it has become clear that this convenient empirical diagnostic begins to break down as one assembles larger (and generally fainter) samples of SNRs, and in particular as one also compares with fainter and perhaps more typical H II regions. Below, we consider two different regimes where confusion in applying the $[\text{S II}]:\text{H}\alpha$ ratio criterion occurs.

6.1. Are the Candidates That Have $[\text{S II}]:\text{H}\alpha < 0.4$ Likely to Be SNRs?

As shown in the left panel of Figure 5, applying a ratio of 0.4 across the sample raises a number of questions. As discussed earlier, Winkler et al. (2017) identified a small number of SNR candidates whose GMOS spectra showed ratios below the 0.4 threshold (see their Figure 6). In Winkler et al. (2017), we argued that most of these nebulae should still be regarded as good candidates, because (a) there was other information that suggested they were SNRs, (b) not all shocks have $[\text{S II}]:\text{H}\alpha$ ratios greater than 0.4, or (c) uncertainties in the measurements made their actual ratios uncertain. These objects were examined and determined to be good SNR candidates despite the low ratios. Have we altered our opinion, based on the new MUSE observations? Our answer is no, for a combination of observational and theoretical reasons.

There are numerous bright candidates for which the MUSE-derived ratio is below 0.4. Two significant but related factors that could contribute to this are (a) contamination by coincident H II emission and (b) uncertainties in background subtraction. It turns out that of the 20 candidates with high surface brightness that do not pass the $[\text{S II}]:\text{H}\alpha \geq 0.4$ criterion, nearly all are in the nuclear region where both of the above problems are most extreme. Our choice to take a background from the area of lowest surface brightness within $5''$ of the SNR candidate is conservative in the sense that we avoid oversubtracting the background, but it means that we are sensitive to emission that lies very close to the SNR, especially as these sources, many of which were discovered on the basis of the $[\text{Fe II}]$ emission, are faint in the optical. Even though the MUSE observations were taken under good ($0''.7$) seeing, a definitive assessment of the nature of these objects really requires the angular resolution of HST.

Figure 8 shows a cluster of SNRs from Blair et al. (2012) embedded in the extended emission region in the spiral arm to the southwest of the M83 nucleus, as they appear in the Magellan imaging data and with MUSE. The objects of interest are seen in the Magellan ratio map with modestly enhanced ratios relative to surrounding emission. However, the MUSE ratio map shows less enhancement for a number of these objects despite the narrower MUSE bandpasses extracted, as discussed in Section 3.1. Possibly, the $0''.7$ resolution of the MUSE data is just enough poorer than the $0''.4$ – $0''.5$ resolution of the Magellan IMACS data that smearing and H II region contamination lower the observed ratios. Though the problem is not as severe as in the nuclear region, our belief is that these objects remain viable candidates, especially factoring in the Magellan results.

Furthermore, Kopsacheili et al. (2020) have carried out a reexamination of the optical line ratios that might serve to

identify SNRs in nearby galaxies by comparing the theoretical line ratios produced by the shock models of Allen et al. (2008) to two sets of photoionization models of gas around starbursts created by Kewley et al. (2001) and Levesque et al. (2010). Both the shock and the photoionization models were carried out with Mappings (Sutherland & Dopita 1993; Allen et al. 2008) and therefore should be directly comparable. Kopsacheili et al. (2020) note that a large number of the shock models have $[\text{S II}]:\text{H}\alpha$ ratios less than 0.4, and in particular that using 0.4 as a strict cutoff disfavors the identification of SNRs with slow shock velocities.¹⁵ If these shocks are realized in nature, then one should continue to study the set of objects that have $[\text{S II}]:\text{H}\alpha$ ratios that are somewhat elevated compared to H II regions to see whether there are other indicators that they actually are shocks.

We note in passing that Kopsacheili et al. (2020) argue that various combinations of line ratios involving $[\text{O I}]$, $[\text{O II}]$, $[\text{O III}]$, $[\text{N II}]$, and $[\text{S II}]$ provide a more accurate way to identify all nebulae with shocks. A full analysis of all of these possibilities for the MUSE spectra is beyond the scope of this paper and would not be straightforward owing to the large range in S/N of the various spectra. As an example of the difficulties, we note that Kopsacheili et al. (2020) argue that the cleanest single line for identifying shocks is the $[\text{O I}]:\text{H}\alpha$ ratio; of the models they investigate, 97% of shocks had a ratio greater than 0.017, but only 2.4% of the starburst models satisfied this ratio. The observational problem, of course, is that measuring $[\text{O I}]$ to a precision that is such a small percentage of $\text{H}\alpha$ is difficult, which is why we used a value of 0.1 above as a secondary indicator that a nebula was shock dominated. Also, while the statistics Kopsacheili et al. (2020) quote are correct in terms of what the models predict, the relative number of instances of each model in nature is unlikely to be flat. In the case of the M83 sample, 113 of the 160 SNR candidates satisfying the $[\text{S II}]:\text{H}\alpha$ criterion of 0.4 also have $[\text{O I}]:\text{H}\alpha$ greater than 0.1, but only three of the other candidates have a measured $[\text{O I}]:\text{H}\alpha$ greater than 0.1. By contrast, for the H II sample of 188 objects, 14 have $[\text{O I}]:\text{H}\alpha$ greater than 0.1; if Kopsacheili et al. (2020) actually reflected nature, these objects would be classified as SNRs.

6.2. Are Faint Objects with $[\text{S II}]:\text{H}\alpha > 0.4$ Likely to Be SNRs?

Transitioning to the fainter end of the distribution, over the past decade new SNR surveys have pushed to lower surface brightness, and the gap in ratio between H II regions and SNRs has closed to the point where the middle ground is muddled. Thus, one needs to consider the possibility that some of the emission nebulae we are identifying as SNRs are really just bright patches in the DIG that exists in the more distributed ISM. Despite having very low surface brightness in $\text{H}\alpha$, the DIG competes with H II regions in terms of the total $\text{H}\alpha$ luminosity emitted by a galaxy because of its spatial extent. Observationally (see, e.g., Haffner et al. 2009, for a review), the DIG has many of the same properties as gas in SNRs, specifically high $[\text{S II}]:\text{H}\alpha$ ratios that correlate inversely with low surface brightness (Galarza et al. 1999). As measured by Della Bruna et al. (2022a), the radially averaged surface brightness of the DIG in M83 is in the range $(2 - 2.5) \times 10^{-16}$ ergs $\text{cm}^{-2} \text{s}^{-1} \text{arcsec}^{-2}$.

¹⁵ One caveat to this conclusion is the absence of shock models below 100 km s^{-1} in the Allen et al. (2008) model grid.

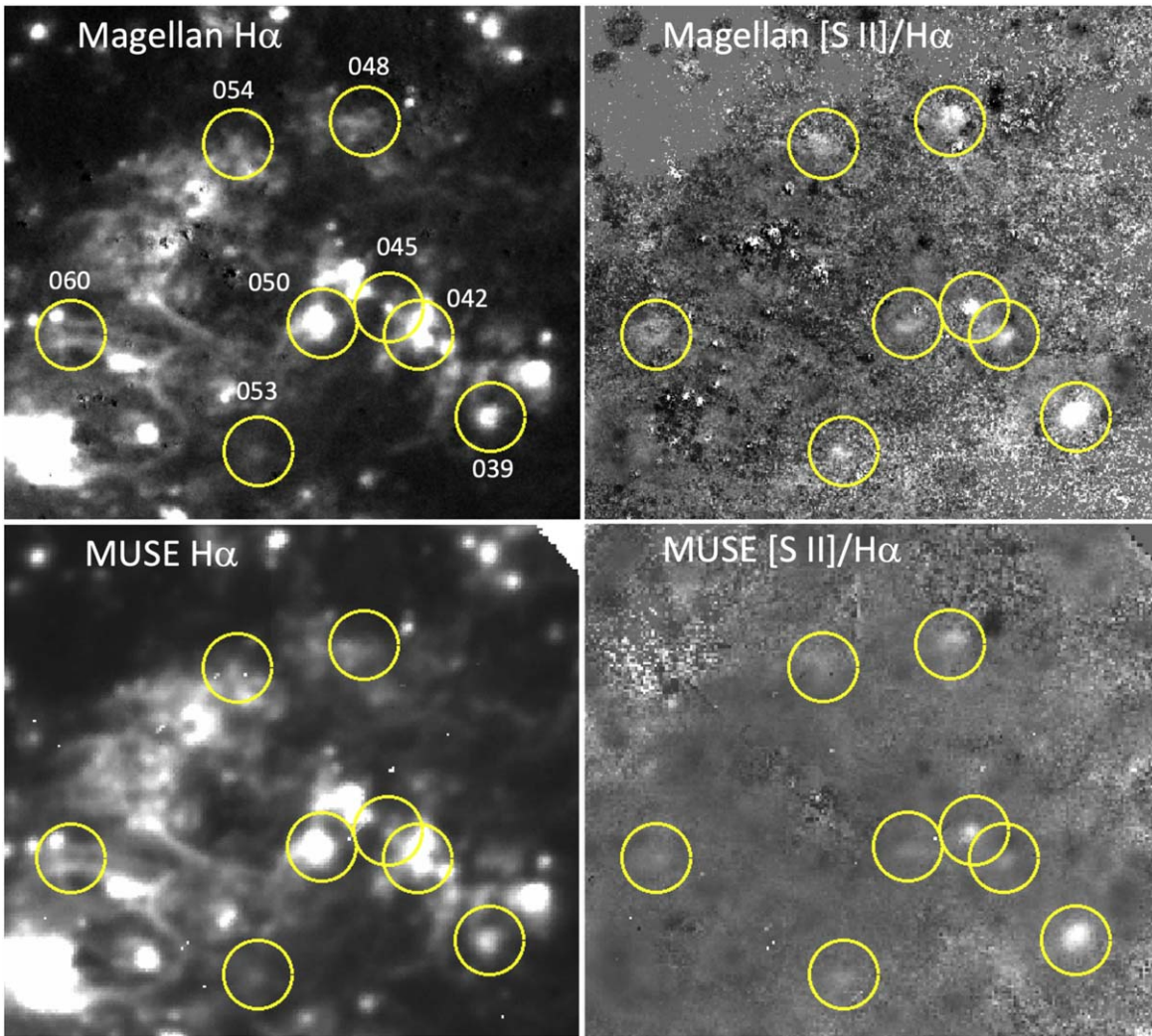


Figure 8. A figure similar to Figure 2 showing a $\sim 35''$ region in the southwest spiral arm of M83. The yellow circles indicate previous SNRs from Blair et al. (2012), with numbers in the top left panel indicating their identifications in that catalog. These objects are embedded in extended $H\alpha$ emission at various levels, and their $[S II]:H\alpha$ ratios are only modestly enhanced in the Magellan ratio map. However, most of these objects are even less enhanced in the MUSE ratio map, likely due to the somewhat lower spatial resolution (and hence additional contamination) of the MUSE data. This effect also impacts the observed ratios in the extracted MUSE spectra for such objects. The scaling on the ratio maps is from 0 (black) to 1.5 (white).

One way to assess how serious this problem might be is to compare the $[S II]:H\alpha$ ratios obtained from the background-subtracted spectra of the SNR candidates to those of the spectra obtained from the background regions themselves, which is shown in Figure 9. A number of trends are apparent: (1) The $[S II]:H\alpha$ ratios of the background regions show a pronounced trend toward higher ratios at low surface brightness. If these background regions were well-defined nebulae, which they are not,¹⁶ many would be regarded as viable SNR candidates. (2) A number of the faint SNR candidates have very high $[S II]:H\alpha$ ratios compared to the main locus of background points at the same surface brightness, which is encouraging. However, the 34 SNR candidates with a surface brightness of $< 10^{-16}$ ergs cm^{-2} s^{-1} arcsec $^{-2}$ are typically only a few times as bright as the background that is being subtracted from them.

¹⁶ Recall that the difference between the background regions and the faint SNR candidates we have identified is that the SNR candidates were identified as coherent, identifiable emission regions whereas the background regions could be random locations within $5''$ of the nominal SNR coordinate. Hence, the background regions have systematically lower surface brightness and could well be representative of DIG in many cases.

We have checked to see whether there are other properties that might distinguish the faint SNR candidates from the DIG, as represented by the background regions. The measured widths of $H\alpha$ and the $[O III]:H\beta$, $[O I]:H\alpha$, and $[N II]:H\alpha$ ratio distributions are fairly similar. One might hope to distinguish low surface brightness SNRs from the (photoionized) DIG based on the shape of the line profiles, but with a few exceptions, the low surface brightness candidates have lines that are unresolved at the MUSE resolution. Hence, the identification of the faint objects as SNRs depends fairly critically on their being identified as well-defined nebulae. For these reasons, even though the faint objects have the spectroscopic characteristics of SNRs, it seems likely that some fraction of them could be misidentified.

6.3. The Bottom Line

As SNR surveys in nearby galaxies have pushed to lower surface brightnesses, the oft-used observational discriminant of observed $[S II]:H\alpha \geq 0.4$ to indicate shock-heated nebulae has become less deterministic. While it remains true that bright

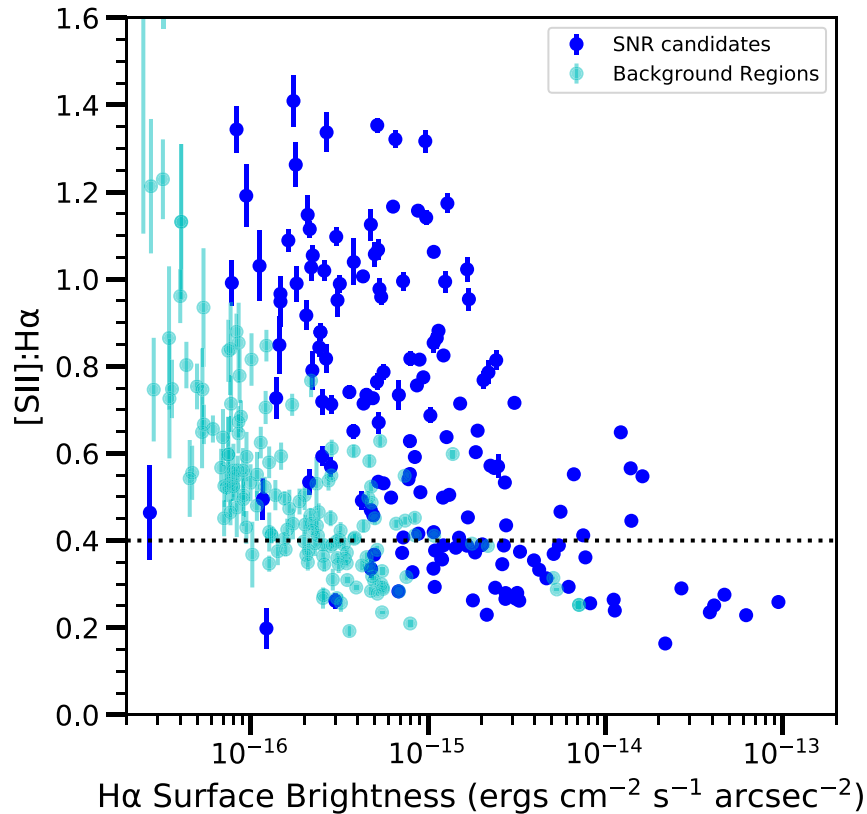


Figure 9. The [S II]:H α ratios of SNR candidates observed with MUSE compared to those of the spectra obtained from the background regions associated with the SNR candidates. Emission nebulae with [S II]:H α ratios greater than 0.4 are normally considered good SNR candidates. However, at lower surface brightness levels, the ratio rises into the nominal SNR range, indicating that the normal value may not be applicable. See text for details.

photoionized nebulae typically have low values of this ratio, at lower surface brightnesses this is no longer the case and observed ratios can meet or exceed the normal threshold to indicate shock heating. Of course, observational error in determining the ratio also increases for the faintest nebulae, and the proper removal of any overlying background emission also becomes more problematic. Also, referring to grids of shock model calculations where many variables come into play, it is clear that there are regions of parameter space where shocked nebulae do not necessarily produce a ratio above 0.4, although this remains true for a wide portion of the expected parameter space for shocks.

We and others, including Kopsacheili et al. (2020), have investigated various secondary criteria that appear to be useful in specific cases to help confirm shock heating in optically identified candidates, but none of these provide a silver bullet, especially for the faintest nebulae identified with the optical criterion. For example:

1. The presence of a coincident soft X-ray or nonthermal radio source is a strong confirmation of shock heating and is even a primary diagnostic for SNRs in our Milky Way. However, these emissions are typically observable only for the brighter objects in nearby galaxies, even with lengthy integrations.
2. The presence of additional shock-heated line enhancements such as [O I]/H α , [N II]/H α , and [Fe II]/H α , or even the relatively new criterion used in this paper, [S III]/[S II], can again help confirm in some individual cases, but they are in many ways similar to the [S II]/H α

criterion in that they are variable with shock conditions and hence model dependent.

3. The kinematic diagnostic should in principle be fairly deterministic; photoionized gas should show thermal broadening that is only at the 10–20 km s $^{-1}$ level, while bulk motions from shocks should produce much broader line profiles. However, with only modest kinematic resolution of ~ 100 km s $^{-1}$ that is usually available, there is still the potential for indeterminate results for lower-velocity shocks. Obtaining even higher spectral resolution data would be beneficial, but for exceedingly faint nebulae, this is a difficult task.

All of this is to say that the goal of achieving a complete survey of the SNR population within a given external galaxy is very difficult to achieve. The veracity of our SNR identifications is quite strong for the brighter objects, while the identifications at lower surface brightnesses must be considered provisional in many cases.

7. Special Objects of Interest

In a recent paper discussing some of the M83 SNR candidates that seemed to have peculiar morphology, Soria et al. (2020) concluded that there was a pair of adjacent SNR candidates, B12-096 and B12-098, that were likely two lobes from a single microquasar. A hard stretch of the HST H α image further shows a jet-like extension from B12-098 to the E–SE. The MUSE spectra of the bright emission from these two objects show similar spectra that confirm high [S II]:H α ratios and moderately high [S II] densities for both lobes. [N II]

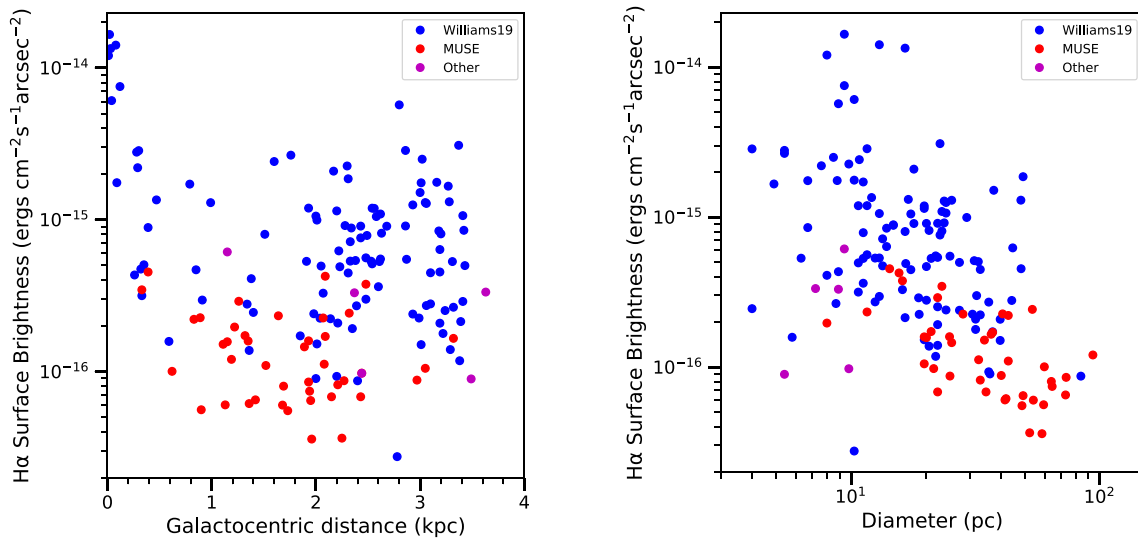


Figure 10. Left: $H\alpha$ surface brightness as a function of galactocentric distance for SNR candidates with $[S II]:H\alpha$ ratios greater than 0.4. Right: $H\alpha$ surface brightness as a function of object diameter for the same objects.

$\lambda 6543$ is comparable to or slightly weaker than $H\alpha$, and $[O III] \lambda 5007$ is comparable to or stronger than $H\alpha$. In the extended red coverage provided by MUSE, $[S III] \lambda 9072$ is clearly detected in both objects. These spectra are thus consistent with shock heating of these lobes with shock velocities in excess of 100 km s^{-1} . This situation may be similar to that observed in the W50/SS433 microquasar system in our own Galaxy (Dubner et al. 1998 and references therein). This object may be a more evolved version of the first M83 microquasar that was detected just NE of the nuclear region (Soria et al. 2014).

Another object worthy of mention is B12-174a, an apparently very young SNR (≤ 100 yr) that shows very high velocity ($\sim 5000 \text{ km s}^{-1}$) emission features in its spectrum (Blair et al. 2015). B12-174a is a bright compact emission knot that appears in projection against the northern limb of a larger, lower surface brightness SNR candidate, B12-174. The MUSE B12-174a spectrum is shown in Figure 3 and indicates the presence of narrow lines in addition to the broad red emission feature that encompasses the entire $H\alpha$ – $[N II]$ – $[S II]$ region. The MUSE spectrum of the larger shell, B12-174, confirms a shock-heated spectrum, but the flux from this larger SNR is too faint to account for the narrow emission lines seen at the B12-174a position.

Since these narrow lines show somewhat elevated $[S II]:H\alpha$ and $[N II]:H\alpha$, it would be interesting if they were intrinsic to the young SNR, perhaps indicating a shock precursor or other low-velocity shock emission in addition to the broad component. However, these narrow lines were not seen by Blair et al. (2015). We have reviewed the GMOS data, which were obtained with a $1''.25 \times 6''$ slitlet in good seeing. Performing spatial and spectral crosscuts in the 2D GMOS spectra, we do not find evidence of narrow emission associated directly with the compact SNR, although variable narrow emission overlays the entire region. We conclude that the narrow features in the MUSE spectrum are most likely residual background emission that is along the line of sight to the object. There is little or no difference in the shape of the broad red component in the MUSE and GMOS spectra of B12-174a, although, given the quality of both spectra, the changes would have to have been fairly large to have been detected. No new broad features were

detected in the extended red spectral coverage provided by MUSE.

8. Global Trends in the MUSE Spectra of SNRs in M83

Given such a large and homogeneous sample of spectra, it is important to try to understand any systematic trends in the characteristics they display. For this purpose, we consider only those SNR candidates that have $[S II]:H\alpha$ ratios greater than 0.4 and therefore are most likely to be SNRs. Figure 10 shows the surface brightnesses of these objects as a function of galactocentric distance and object diameter. Except in the nuclear region where the background is very high, there is no obvious trend of surface brightness with galactocentric distance. This is consistent with the idea that the surface brightness of an SNR is dependent on local conditions, not global ones. By contrast, there is a clear correlation between surface brightness and SNR diameter. This is at least partially a physical effect: while smaller-diameter objects with low surface brightness, and hence low total flux, are unlikely to have been identified, larger-diameter, high surface brightness objects would certainly have been found if present, and none are seen. The most straightforward explanation for this is that high surface brightness suggests high density and the shocks of SNRs expanding into higher density evolve more rapidly than those expanding into lower density and thus simply evolve beyond the radiative phase before reaching a large diameter.

Support for the idea that smaller-diameter objects tend to be expanding into denser media on average is provided by the density-sensitive line ratio of $[S II] \lambda 6716:\lambda 6731$. Although the scatter is significant, Figure 11, shows that objects with higher surface brightness (left panel) and smaller diameter (right panel) tend to have lower $[S II] \lambda 6716:\lambda 6731$ ratios, which implies higher densities. The addition of the newly discovered MUSE low surface brightness sample tends to solidify these conclusions: although the observational errors increase for these faint objects, many are at or above the nominal low-density limit of the ratio in the plot.

Most of the objects in the SNR sample show evidence for a moderate amount of reddening as shown in Figure 12. The galactic foreground extinction should be small ($E(B - V) = 0.059$;

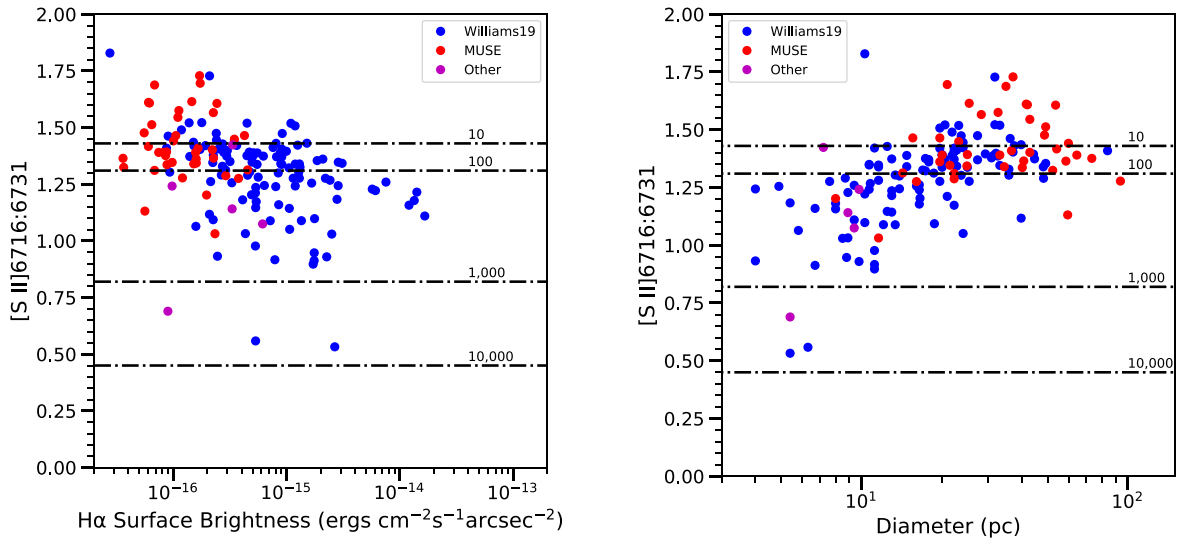


Figure 11. Left: the density-sensitive [S II] $\lambda 6716:\lambda 6731$ ratio as a function of $H\alpha$ surface brightness for SNR candidates with [S II]: $H\alpha$ ratios greater than 0.4. Right: [S II] $\lambda 6716:\lambda 6731$ as a function of object diameter. The dashed lines show the expected ratios for various electron densities (Osterbrock & Ferland 2006).

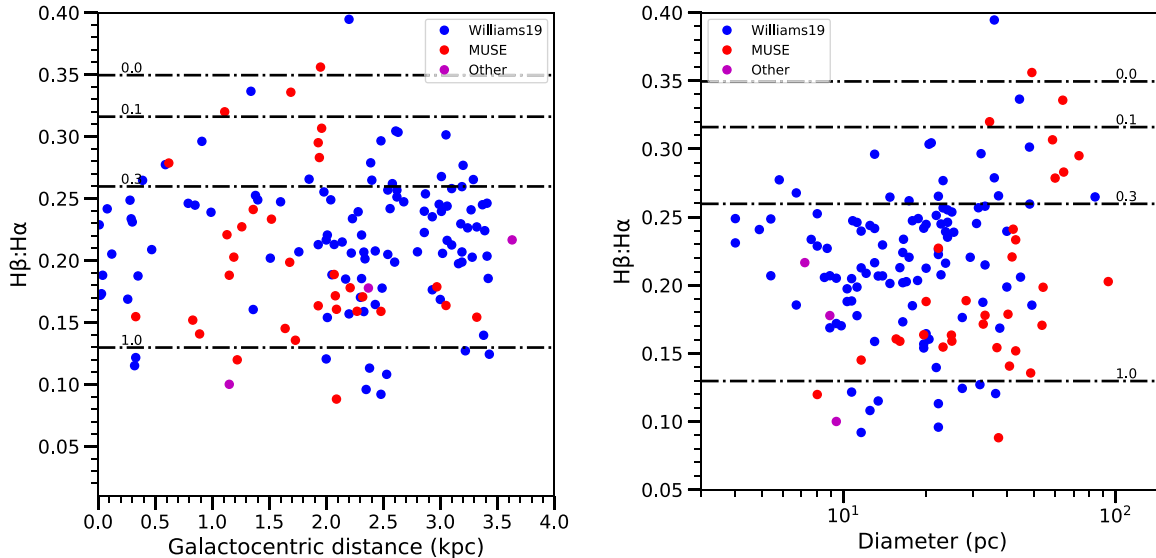


Figure 12. Left: $H\beta:H\alpha$ as a function of galactocentric distance for SNR candidates with [S II]: $H\alpha$ ratios greater than 0.4. Right: $H\beta:H\alpha$ as a function of object diameter. The dashed lines show the expected $H\beta:H\alpha$ ratios for various values of $E(B - V)$ (Seaton 1979).

Schlafly & Finkbeiner 2011), so the very low values seen for a few objects likely point to a small amount of observational error. There are no obvious trends in the amount of reddening with either galactocentric distance or diameter, as expected since extinction effects should be dominated by very local conditions impacting the individual objects. The range seen here is directly comparable to Figure 7 of Winkler et al. (2017) from the GMOS spectroscopy. The newly identified MUSE objects span the entire range of extinction seen in the earlier sample, although, once again, the uncertainties are larger for these faint objects, especially in measuring the $H\beta$ line in the more reddened objects.

As shown in Figure 13, correlations between FWHM of $H\alpha$ as a function of surface brightness and diameter are weak. That said, the range of FWHM for objects with diameters less than 20 pc is clearly larger than the range of FWHM for objects larger than this. The FWHMs in the spectra represent the dispersion in the bulk velocity of the shocked material in an

SNR (since the thermal velocity of material behind the shock is small). In principle, therefore, one could get a low FWHM with a high-velocity shock, if all of the emission came from a single shocked cloud at the edge of an SNR. However, if the shocked material is distributed at various positions around the periphery, it is more likely that the FWHM correlates with the typical shock velocity. Thus, the large dispersion in FWHM at smaller diameters is consistent with the interpretation that many of these SNRs have encountered higher-density gas than others. The objects at large diameters have all evolved to the point where the shock velocity is relatively low.

While the scatter is large, objects that exhibit a large FWHM in $H\alpha$, and hence higher shock velocities, tend to have [S II] $\lambda 6716:\lambda 6731$ ratios associated with higher density, as one would expect if SNe explode and eject (to an order of magnitude or so) the same amount of energy into the ISM in the form of shocks. If the ISM is dense, the SNR will evolve to

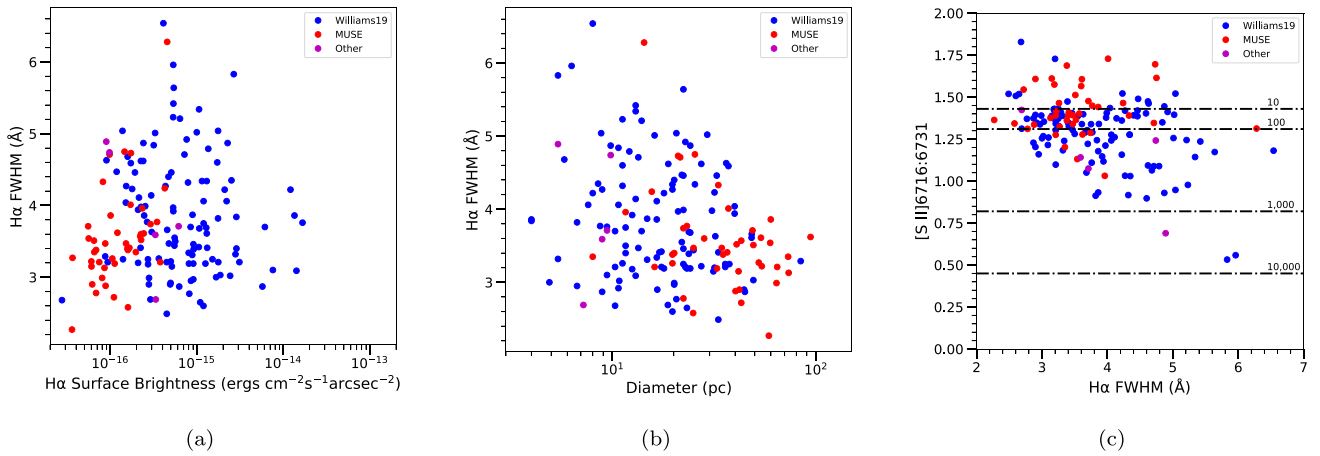


Figure 13. (a) H α FWHM as a function of H α surface brightness for SNR candidates with [S II]:H α ratios greater than 0.4. (b) H α FWHM as a function of object diameter. (c) The density-sensitive [S II] λ 6716: λ 6731 ratio as a function of H α FWHM.

the limit of detectability relatively quickly and the energy will be radiated away on a relatively short period of time. If the ISM is tenuous, the SNR will become detectable later, when the velocity of the primary shock is lower. SNRs expanding into dense media reach the radiative phase at smaller diameters, after which they begin to fade. The optical emission from SNRs arises primarily from secondary shocks that are driven into the denser regions of the ISM, as is evidenced by the fact that the optical and X-ray appearances of resolved SNRs are usually quite different. However, there is rough pressure equilibrium between the primary and secondary shocks, since the secondary shocks are driven by the pressure mismatch between the X-ray gas and the cool clouds. Therefore, we expect that small-diameter SNRs will tend to show higher densities and higher velocity widths than larger objects.

9. Comparison to Models

The emission seen from a typical SNR in M83 represents emission from a large number of shocks traversing material with a range of densities in local circumstellar (for small objects) and/or interstellar material. Therefore, the line ratios that are observed are not expected to correspond exactly to those obtained from calculations based on a single shock velocity and density. Nevertheless, comparisons to theoretical models have typically proven useful for characterizing the global spectra of extragalactic SNRs.

Figure 14 shows grids of the expected line ratios of [O III]:H β versus [N II] λ 6583 and [N II] λ 6583:H α versus [S II]:H α from a series of shock models calculated by Allen et al. (2008) using the Mappings III code. The discrete points show the results from our spectra. The model grids span a range of shock velocity from 100 to 1000 km s $^{-1}$ and pre-shock magnetic field from 10 $^{-4}$ to 10 μ G, with different colors representing abundance sets that are appropriate for LMC, solar, and twice-solar values. All of the models are for a pre-shock density of 1 cm $^{-3}$, and all ignore precursor ionization of the ISM.¹⁷

A number of trends can be seen in Figure 14. First, none of the observations fall within the locus of the models created with

subsolar LMC abundances, in contrast to a similar comparison for SNRs in M33, which has abundances that are about 1/2 solar (Long et al. 2018). Rather, nearly all of the observed data points fall within the region described by theoretical line ratios in the solar or twice-solar [N II] λ 6583:H α versus [S II]:H α diagram, including those candidates that do not satisfy the normal [S II]:H α criterion. This is expected since, according to Bresolin et al. (2016), M83 has an oxygen metallicity of 9.0, or 2.2 \times solar in the nuclear region, and 8.8 (1.5 \times solar) at 0.4 R25. However, nearly all the objects that do not satisfy the [S II]:H α criterion have very low [O III]:H β ratios compared to models in the twice-solar grid. In both of these diagnostic plots, there is a general correlation of the observed spectra between the ratio of [O III]:H β versus [S II]:H α and [N II]:H α versus [S II]:H α .

As we have noted earlier, Kopsacheili et al. (2020) have pointed out that many of the Allen et al. (2008) shock models have [S II]:H α ratios of less than 0.4. This is evident in Figure 14. On the other hand, most of the SNR candidates we have observed in M83 with MUSE that have low [S II]:H α ratios have [O III]:H β ratios that fall outside the locus of the theoretical models. To the extent that one has faith in the models, this would argue that the objects with low [S II]:H α ratios are not SNRs.

An alternative possibility is that these SNRs have emission that is dominated by lower shock velocities than available in the comparison model grid. The Allen et al. (2008) models only start at 100 km s $^{-1}$ and go up. At lower shock velocities, it could be that oxygen never gets ionized to O $^{++}$, and hence little [O III] emission is present. This is consistent with the discussion from Blair et al. (2014), where many of the SNRs in M83 become bright and radiative at small diameters owing to a high-density, high-pressure ISM. By the time the SNRs expand to intermediate and larger diameters, the shock velocity decreases and the ionization goes down. This explanation is also consistent with the trends noted above (e.g., lower surface brightness and lower densities for larger-diameter SNRs).

10. Summary and Conclusions

Historically, SNRs in external galaxies have been identified using narrowband interference-filter imaging to identify candidates, and with moderate-resolution spectroscopy to confirm that the candidate objects have high [S II]:H α ratios

¹⁷ Allen et al. (2008) also calculated models allowing for precursor ionization. The main difference qualitatively is that, at least for solar and twice-solar abundances, the [N II] λ 6583:H α ratios are lower and the [O III]:H β ratios are somewhat higher. The [O III]:H β ratios of objects that fail the [S II]:H α criterion still fall outside the range of the models.

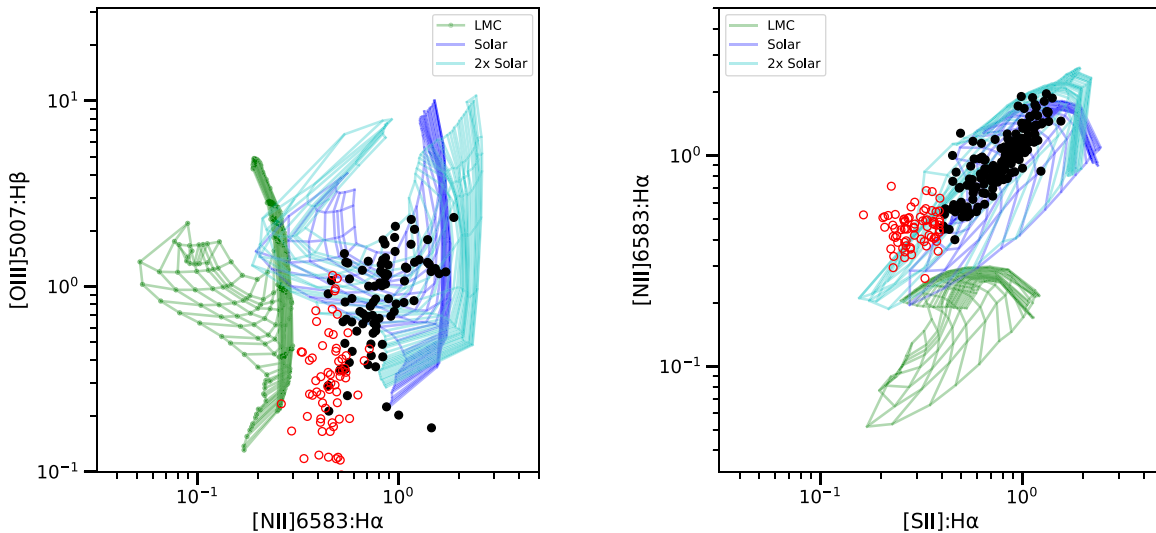


Figure 14. Left: observed $[\text{O III}] \lambda 5007:\text{H}\beta$ ratio as function of the $[\text{N II}] \lambda 6583:\text{H}\alpha$ line ratio for M83 SNRs and SNR candidates with spectra compared with model grids from Allen et al. (2008). As discussed in the text, the green, blue, and cyan meshes correspond to shock models with a range of shock velocities and pre-shock magnetic fields, and with metallicities corresponding to LMC (green), solar (blue), and twice solar (cyan), respectively. Candidates that satisfy the $[\text{S II}]:\text{H}\alpha$ criterion are plotted in black; those that fail this test are plotted as open red circles. Right: the same comparison for $[\text{N II}] \lambda 6583:\text{H}\alpha$ line ratios as a function of the $[\text{S II}]:\text{H}\alpha$ ratios.

compared to H II regions. In M83, after the corrections noted in Section 3, the Williams et al. (2019) list contained 278 SNR and candidates, of which 118 had spectra (Winkler et al. 2017). Of these, 103 had $[\text{S II}]:\text{H}\alpha$ ratios that exceeded 0.4, the dividing line most often utilized to declare an SNR candidate as a bona fide SNR in the optical.

Here, we have used a mosaic of MUSE data for M83, as assembled by Della Bruna et al. (2022a), along with our earlier HST and Magellan images of M83 to update and study the SNRs in M83. Our new catalog of SNRs contains 366 objects, of which 81 have not been reported previously, including 44 SNR candidates obtained by inspection of narrowband images extracted from the MUSE data cube.

There are 229 of these catalog objects contained within the region observed with MUSE, 170 of which have never previously been observed spectroscopically, making a substantial step forward in characterizing the overall SNR population. We have extracted spectra for all candidates, and our analysis shows that 160 have $[\text{S II}]:\text{H}\alpha$ ratios greater than 0.4. Of the objects that satisfy this criterion, 137 also show lines that are broadened beyond that seen in a sample of H II regions, and 150 have a ratio of $[\text{S III}]:[\text{S II}]$ less than 0.2, as expected for shocked gas. Many are also associated with Chandra-detected X-ray sources (Long et al. 2014). By all preexisting standards these objects are SNRs. If we add SNR candidates outside the MUSE region that have spectroscopically determined $[\text{S II}]:\text{H}\alpha$ ratios greater than 0.4, then 211 SNRs have been confirmed in M83 out of the 288 that have been observed spectroscopically with either GMOS or MUSE. Most of the others that have spectra with measured $[\text{S II}]:\text{H}\alpha$ ratios well in excess of the value of 0.1 are usually associated with bright H II regions, but their true nature remains more uncertain.

These results contrast with MUSE spectra extracted for a set of 188 nebulae, nominally H II regions, which were selected as random faint isolated patches of $\text{H}\alpha$ emission. These nebulae were intended to span the range of surface brightnesses in the SNR candidate sample to make a valid comparison. Overall, the $[\text{S II}]:\text{H}\alpha$ ratios for this sample were low, as expected; only seven

of these randomly selected nebulae turned out to have an $[\text{S II}]:\text{H}\alpha$ ratio greater than 0.4, only 14 had a measured FWHM of $\text{H}\alpha$ greater than 3 \AA , and only 14 showed believable $[\text{O I}]$ emission.

Limiting ourselves to the most confident set of SNR candidates for which the $[\text{S II}]:\text{H}\alpha$ ratio was observed to be greater than 0.4, we find a number of trends:

1. The mean surface brightness in $\text{H}\alpha$ declines with diameter, but (excluding the nuclear region) not with galactocentric distance. In the nucleus, bright background limits sensitivity, and so the objects we can identify are systematically brighter there.
2. The observed density-sensitive $[\text{S II}] \lambda 6716:\lambda 6731$ ratios increase with SNR diameter, indicating that the optical shocks seen in small-diameter objects are, on average, encountering denser material than those in large-diameter objects.
3. SNRs with smaller diameters ($<10 \text{ pc}$ as measured on HST images) have $\text{H}\alpha$ line widths that span a larger range than those that have larger diameters. This is consistent with diverse CSM/ISM environments surrounding the younger objects.
4. SNRs with higher $\text{H}\alpha$ line widths tend to be dominated by shocks with $[\text{S II}] \lambda 6716:\lambda 6731$ ratios that indicate higher densities. This is expected if the post-shock pressure is proportional to the shock velocity squared and the temperature of the $[\text{S II}]$ emission zone is always at a temperature of about 10,000 K.

These trends are largely consistent with the idea that small-diameter objects can be small either because they are “younger” in an evolutionary sense or because they are encountering denser gas and hence evolving more rapidly. The large-diameter objects must have been the result of SNe that exploded in regions with more tenuous gas, so that that they could expand to a larger size before becoming radiative and then fading away.

Compared to SNRs identified in other galaxies and to models of shocks in SNRs, the spectra of SNRs in M83 show relatively

low [O III]:H β ratios. This may point to a population of SNRs in M83 with relatively low shock velocities that cannot ionize the gas to O⁺⁺.

Finally, as a coda to this study, we note that relatively wide field, high spectral and spatial resolution integral field spectrographs on large telescopes and with wide wavelength coverage, like MUSE, are certain to be increasingly important for future optical studies of SNRs in nearby galaxies. This is in part because IFU spectrographs allow a cleaner separation of the relevant emission lines than is possible with the narrowband interference-filter imaging that has historically been used to identify SNR candidates in nearby galaxies. The broad wavelength coverage makes available additional lines, in this case [S III] λ 9069, to help discriminate shock-heated from photoionized gas. And most importantly, high spectral resolution allows one to identify SNRs kinematically, which is required to distinguish shock-heated from photoionized gas in fainter objects, since the line ratios seen from the DIG resemble closely those expected from shock-heated material. The fundamental limitation, of course, is that to learn much about the global evolutionary properties of SNRs in external galaxies, one also needs to measure their diameters, which beyond the Local Group requires high spatial resolution imaging such as can be obtained with HST.

Based primarily on observations collected at the European Southern Observatory under ESO programmes 096.B-0057(A), 0101.B-0727(A), 097.B-0899(B), and 097.B-0640. K.S.L. acknowledges partial support from the Space Telescope Science Institute, which is operated by AURA, Inc., under NASA contract NAS 5-26555. P.F.W. acknowledges support from the NSF through grant AST-1714281. W.P.B. acknowledges partial support from the JHU Center for Astrophysical Sciences during the time of this work. A.A. acknowledges the support of the Swedish Research Council, Vetenskapsrådet, and the Swedish National Space Agency (SNSA). Finally, we appreciate the advice of an anonymous referee, whose careful reading allowed us to improve the final version of the manuscript.

Facilities: VLT/MUSE, HST/WFC3, Magellan/IMACS.

Software: astropy (Astropy Collaboration et al. 2013).

ORCID iDs

Knox S. Long  <https://orcid.org/0000-0002-4134-864X>
 William P. Blair  <https://orcid.org/0000-0003-2379-6518>
 P. Frank Winkler  <https://orcid.org/0000-0001-6311-277X>
 Angela Adamo  <https://orcid.org/0000-0002-8192-8091>
 Anna F. McLeod  <https://orcid.org/0000-0002-5456-523X>
 Phillippe Amram  <https://orcid.org/0000-0001-5657-4837>

References

- Allen, M. G., Groves, B. A., Dopita, M. A., Sutherland, R. S., & Kewley, L. J. 2008, *ApJS*, **178**, 20
- Astropy Collaboration, Robitaille, T. P., Tollerud, E. J., et al. 2013, *A&A*, **558**, A33
- Bacon, R., Accardo, M., Adjali, L., et al. 2010, *Proc. SPIE*, **7735**, 773508
- Blair, W. P., Chandar, R., Dopita, M. A., et al. 2014, *ApJ*, **788**, 55
- Blair, W. P., Kirshner, R. P., & Chevalier, R. A. 1981, *ApJ*, **247**, 879
- Blair, W. P., & Long, K. S. 2004, *ApJS*, **155**, 101
- Blair, W. P., Winkler, P. F., & Long, K. S. 2012, *ApJS*, **203**, 8
- Blair, W. P., Winkler, P. F., Long, K. S., et al. 2015, *ApJ*, **800**, 118
- Boissier, S., Gil de Paz, A., Madore, B. F., et al. 2005, *ApJL*, **619**, L83
- Bresolin, F., Kudritzki, R.-P., Urbaneja, M. A., et al. 2016, *ApJ*, **830**, 64
- Cappellari, M. 2017, *MNRAS*, **466**, 798
- Cappellari, M., & Emsellem, E. 2004, *PASP*, **116**, 138
- Della Bruna, L., Adamo, A., Amram, P., et al. 2022a, *A&A*, in press (arXiv:2202.01738)
- Della Bruna, L., Adamo, A., McLeod, A. F., et al. 2022b, *A&A*, submitted
- D’Odorico, S. 1978, *MmSAI*, **49**, 485
- Dopita, M. A., Blair, W. P., Long, K. S., et al. 2010, *ApJ*, **710**, 964
- Dubner, G. M., Holdaway, M., Goss, W. M., & Mirabel, I. F. 1998, *AJ*, **116**, 1842
- Galarza, V. C., Walterbos, R. A. M., & Braun, R. 1999, *AJ*, **118**, 2775
- Haffner, L. M., Dettmar, R. J., Beckman, J. E., et al. 2009, *RvMP*, **81**, 969
- Jacobs, B. A., Rizzi, L., Tully, R. B., et al. 2009, *AJ*, **138**, 332
- Kewley, L. J., Dopita, M. A., Sutherland, R. S., Heisler, C. A., & Trevena, J. 2001, *ApJ*, **556**, 121
- Kopsacheili, M., Zezas, A., & Leonidaki, I. 2020, *MNRAS*, **491**, 889
- Levesque, E. M., Kewley, L. J., & Larson, K. L. 2010, *AJ*, **139**, 712
- Long, K. S. 2017, in *Galactic and Extragalactic Samples of Supernova Remnants: How They Are Identified and What They Tell Us*, ed. A. Alsabti & P. Murdin (Cham: Springer), 2005
- Long, K. S., Blair, W. P., Godfrey, L. E. H., et al. 2012, *ApJ*, **756**, 18
- Long, K. S., Blair, W. P., & Krzeminski, W. 1989, *ApJL*, **340**, L25
- Long, K. S., Blair, W. P., Milisavljevic, D., Raymond, J. C., & Winkler, P. F. 2018, *ApJ*, **855**, 140
- Long, K. S., Kuntz, K. D., Blair, W. P., et al. 2014, *ApJS*, **212**, 21
- Mathewson, D. S., & Clarke, J. N. 1973, *ApJ*, **180**, 725
- McLeod, A. F., Ali, A. A., Chevance, M., et al. 2021, *MNRAS*, **508**, 5425
- Osterbrock, D. E., & Ferland, G. J. 2006, *Astrophysics of Gaseous Nebulae and Active Galactic Nuclei* (2nd ed.; Sausalito, CA: Univ. Science Books)
- Poetrodjojo, H., D’Agostino, J. J., Groves, B., et al. 2019, *MNRAS*, **487**, 79
- Points, S. D., Long, K. S., Winkler, P. F., & Blair, W. P. 2019, *ApJ*, **887**, 66
- Raymond, J. C. 1979, *ApJS*, **39**, 1
- Russell, T. D., White, R. L., Long, K. S., et al. 2020, *MNRAS*, **495**, 479
- Saha, A., Thim, F., Tammann, G. A., Reindl, B., & Sandage, A. 2006, *ApJS*, **165**, 108
- Schlaflly, E. F., & Finkbeiner, D. P. 2011, *ApJ*, **737**, 103
- Seaton, M. J. 1979, *MNRAS*, **187**, 73
- Shull, J. M., & McKee, C. F. 1979, *ApJ*, **227**, 131
- Soria, R., Blair, W. P., Long, K. S., Russell, T. D., & Winkler, P. F. 2020, *ApJ*, **888**, 103
- Soria, R., Long, K. S., Blair, W. P., et al. 2014, *Sci*, **343**, 1330
- Sutherland, R. S., & Dopita, M. A. 1993, *ApJS*, **88**, 253
- Talbot, R. J. J., Jensen, E. B., & Dufour, R. J. 1979, *ApJ*, **229**, 91
- Vazdekis, A., Koleva, M., Ricciardelli, E., Röck, B., & Falcón-Barroso, J. 2016, *MNRAS*, **463**, 3409
- Williams, B. F., Hillis, T. J., Blair, W. P., et al. 2019, *ApJ*, **881**, 54
- Winkler, P. F., Blair, W. P., & Long, K. S. 2017, *ApJ*, **839**, 83